Monthly Notices
of the
ROYAL ASTRONOMICAL SOCIETY

MNRAS **463,** 2002–2019 (2016)
Advance Access publication 2016 August 19

doi:10.1093/mnras/stw1993

Coevolution of metallicity and star formation in galaxies to $z \simeq 3.7$ – I. A Fundamental Plane

Leslie Hunt,[1]★ Pratika Dayal,[2] Laura Magrini[1] and Andrea Ferrara[3]

[1]*INAF/Osservatorio Astrofisico di Arcetri, Largo Enrico Fermi 5, I-50125 Firenze, Italy*
[2]*Kapteyn Astronomical Institute, University of Groningen, PO Box 800, NL-9700 AV Groningen, the Netherlands*
[3]*Scuola Normale Superiore, Piazza dei Cavalieri 7, I-56126 Pisa, Italy*

Accepted 2016 August 8. Received 2016 August 8; in original form 2016 January 19

ABSTRACT

With the aim of understanding the coevolution of star formation rate (SFR), stellar mass (M_*), and oxygen abundance (O/H) in galaxies up to redshift $z \simeq 3.7$, we have compiled the largest available data set for studying Metallicity Evolution and Galaxy Assembly (MEGA); it comprises ∼1000 galaxies with a common O/H calibration and spans almost two orders of magnitude in metallicity, a factor of $\sim 10^6$ in SFR, and a factor of $\sim 10^5$ in stellar mass. From a principal component analysis, we find that the three-dimensional parameter space reduces to a Fundamental Plane in metallicity (FPZ) given by $12 + \log(\mathrm{O/H}) = -0.14 \log(\mathrm{SFR}) + 0.37 \log(M_*) + 4.82$. The mean O/H FPZ residuals are small (0.16 dex) and consistent with trends found in smaller galaxy samples with more limited ranges in M_*, SFR, and O/H. Importantly, the FPZ is found to be approximately redshift invariant within the uncertainties. In a companion paper, these results are interpreted with an updated version of the model presented by Dayal, Ferrara & Dunlop.

Key words: galaxies: abundances – galaxies: evolution – galaxies: high-redshift – galaxies: star formation.

1 INTRODUCTION

Galaxies are assembled over cosmic time by the accumulation of stellar mass (M_*) through star formation (SF) processes. This build-up is accompanied by an increase of metal content, typically measured through the gas-phase oxygen abundance (O/H), the most abundant heavy element produced by massive stars. Stellar mass is a measure of the integrated SF activity over the history of the galaxy, while the star formation rate (SFR) indicates the current rate for conversion of gas into stars. The gas-phase metallicity (Z) reflects not only the metal production from high-mass stars, but also the level of galaxy interactions with environment through inflows and outflows in the form of galactic winds.

Given the causal relation between SF processes and metal content in galaxies, it is not surprising that M_*, SFR, and O/H are mutually correlated. The mass–metallicity relation (MZR; e.g. Tremonti et al. 2004) is a manifestation of the M_*–Z correlation; the SF 'main sequence' (SFMS) relates M_* and SFR (e.g. Brinchmann et al. 2004; Noeske et al. 2007; Salim et al. 2007). The mutual relations among the three variables extend to specific SFR (sSFR ≡ SFR/M_*) and metallicity which are also correlated (e.g. Salim et al. 2014; Yates & Kauffmann 2014).

These mutual correlations imply that residuals from the main relations (MZR, SFMS) should be correlated with the third variable. Indeed, from an analysis of data from the Sloan Digital Sky Survey (SDSS), Mannucci et al. (2010) found an expression that connected the residuals in the MZR to SFR (see also Ellison et al. 2008); this was dubbed the 'fundamental metallicity relation' (FMR) and reduced the scatter in O/H over ∼80 000 galaxies from ∼0.1 to 0.05–0.06 dex. In a similar vein, Lara-López et al. (2010) showed that the 3D space of M_*, SFR, and O/H for ∼33 000 SDSS galaxies could be expressed through a two-dimensional (planar) surface ('Fundamental Plane', FP). By fitting regressions to parameter pairs, they expressed the FP in terms of M_* and found a residual variation of ∼0.16 dex, larger however than that found for the FMR.

Given that reducing a three-dimensional (3D) parameter space to a (2D) plane is mathematically equivalent to diagonalizing the 3D covariance matrix, a natural approach to this problem is a principal component analysis (PCA). A PCA was first applied to M_*, SFR, and O/H by Hunt et al. (2012) for ∼1000 galaxies from $z \sim 0$–3.5 selected to span a range of $\gtrsim 10^5$ in SFR and two orders of magnitude in O/H.[1] The PCA showed that the principal component dominated by O/H was the component *most dependent* on the other

[1] To avoid problems with the curvature of the MZR at high metallicities, M_* was limited to $\leq$10.5 dex $M_\odot$, so those results are formally applicable only to galaxies less massive than this limit.

★ E-mail: hunt@arcetri.astro.it

two, as by itself it comprised only ∼2 per cent of the total variance. The PCA resulted in an FP in metallicity (FPZ) with a spread of 0.17 dex in O/H, despite the vast range in the original parameters, including redshift. This FPZ applied to the same SDSS samples used by Mannucci et al. (2010, here mass limited) gave roughly the same residuals as the FMR, 0.06 dex. Thus, Hunt et al. (2012) concluded that the FPZ could be used to estimate metallicities with an accuracy of ∼40–50 per cent over an extended range of M_* and SFR, and moreover was a good representation of O/H at $z \gtrsim 3$.

It is now well established that both the MZR and the SFMS extend to the highest redshifts examined so far, but with differing normalizations relative to the Local Universe; at a given M_*, SFR (and sSFR) increases with increasing redshift (e.g. Noeske et al. 2007; Elbaz et al. 2011; Karim et al. 2011; Wuyts et al. 2011; Speagle et al. 2014) while metallicity decreases (e.g. Erb et al. 2006a; Maiolino et al. 2008; Mannucci et al. 2009; Cresci et al. 2012; Xia et al. 2012; Yabe et al. 2012; Henry et al. 2013; Cullen et al. 2014; Steidel et al. 2014a; Troncoso et al. 2014; Wuyts et al. 2014; Zahid et al. 2014; de los Reyes et al. 2015; Ly et al. 2015). Consequently, if we assume that the FPZ is redshift invariant (an assumption that we shall reassess below), the higher sSFRs found in high-z galaxy populations must be related, perhaps causally, to the lower metallicities observed at the same redshift. This is the hypothesis we examine in this paper.

In order to observationally constrain the evolution of metallicity with redshift, we have compiled a new data set of ∼1000 star-forming galaxies from $z \simeq 0$ to $z \sim 3.7$ with nebular oxygen abundance measurements; we will refer to this compilation as the 'MEGA' data set, corresponding to *Metallicity Evolution and Galaxy Assembly*. This compilation is a radical improvement over the data set used by Hunt et al. (2012) because of the inclusion of several more high-z samples and, more importantly, because of a common metallicity calibration. Section 2 describes the 19 individual samples which form the MEGA compilation, together with our estimates of stellar masses and SFRs for the samples at $z \simeq 0$. The procedures for aligning the individual samples to a common O/H calibration are outlined in Section 3. Section 4 describes the scaling relations for the MEGA data set and re-evaluates the redshift invariance of the FPZ through a linear analysis of the correlations of M_*, SFR, and O/H in the MEGA sample and in ∼80 000 galaxies at $z \sim 0$ selected from the SDSS by Mannucci et al. (2010). The coevolution of SFR and O/H with redshift in the MEGA data set is presented in Section 5, together with a comparison of results with previous work. We discuss our results and summarize our conclusions in Section 6. Throughout the paper, we use a Chabrier (2003) initial mass function (IMF) and, when necessary, adopt the conversions for M_* and SFR given by Speagle et al. (2014).

2 GALAXY SAMPLES

Because of the need to compare stellar mass, M_*, SFR, and metal abundance [as defined by the nebular oxygen abundance, 12+log(O/H)], we have selected only samples of galaxies for which either these quantities are already available in the literature or can be derived from published data. Here we discuss the estimates of M_* and SFR; the metallicity determinations for the samples will be discussed in Section 3.

2.1 Local Universe

Four samples of galaxies in the Local Universe met these criteria: the 11 Mpc distance-limited sample of nearby galaxies or Local Volume Legacy (11HUGS, LVL; Kennicutt et al. 2008; Lee et al. 2009, 2011); the Key Insights into Nearby Galaxies: A Far-Infrared Survey with *Herschel* (KINGFISH; Kennicutt et al. 2011); the starburst sample studied by Engelbracht et al. (2008), and the blue compact dwarf (BCD) sample by Hunt et al. (2010). There are 15 galaxies that appear both in the KINGFISH and LVL samples; for these, we used the KINGFISH parameters from Kennicutt et al. (2011) because of the uniform O/H calibration given by Moustakas et al. (2010). The starbursts from Engelbracht et al. (2008) were restricted to only those galaxies (42) with metallicities derived from the 'direct' or 'T_e' method based on electron temperatures (see Table 1 and Section 3); the BCDs (23) all have T_e-measured metallicities.

2.1.1 *Star formation rates*

In order to maximize consistency, we have recalculated SFRs and M_* for the four local samples starting from photometric fluxes reported in the literature. SFRs were derived according to Murphy et al. (2011) using for KINGFISH and LVL the hybrid method with far-ultraviolet (FUV)+total infrared luminosity ($L_{\rm TIR}$); these data were available for 123 (of 138 non-KINGFISH) galaxies with O/H in the LVL and for 50 (of 55) KINGFISH galaxies. For the KINGFISH and LVL galaxies without these data, we adopted other SFR calibrations given by Murphy et al. (2011) including TIR (five galaxies in KINGFISH, six LVL), UV (three LVL), and Hα+24 μm (four LVL). $L_{\rm TIR}$ was calculated according to Draine & Li (2007) and fluxes were taken from Dale et al. (2007, 2009) and Lee et al. (2009, 2011). For 20 LVL galaxies, the SFRs inferred from $L_{\rm TIR}$ were larger than those from FUV+$L_{\rm TIR}$ using the prescriptions by Murphy et al. (2011); in those cases, we adopted SFR($L_{\rm TIR}$). For NGC 253 and M82, SFR($L_{\rm TIR}$) is ∼2 times SFR(FUV+$L_{\rm TIR}$), but for the other galaxies, the two estimates agree to within 30 per cent. We also compared for the LVL galaxies the SFRs calculated with FUV+$L_{\rm TIR}$ with those inferred by combining Hα and 24 μm luminosities ($L_{\rm H\alpha}$, L_{24}; Calzetti et al. 2010; Murphy et al. 2011); SFR(FUV+$L_{\rm TIR}$) tends to be ∼1.6 times larger than SFR(Hα+L_{24}) with a scatter of ∼0.2 dex. This is consistent with the findings of Leroy et al. (2012) who found a similar trend at low surface SFR densities such as those in the LVL galaxies.

Because FUV data are generally not available for the starbursts or the BCDs, for these we adopted the hybrid combination of Hα+L_{24} μm as prescribed by Murphy et al. (2011). Total Hα fluxes were taken from Dopita et al. (2002), Gil de Paz, Madore & Pevunova (2003), James et al. (2004), Pustilnik, Pramskij & Kniazev (2004), Cannon et al. (2005), Moustakas & Kennicutt (2006), Schmitt et al. (2006), López-Sánchez & Esteban (2008), Kennicutt et al. (2008), Cairós et al. (2010), James, Tsamis & Barlow (2010), and 24 μm measurements from Engelbracht et al. (2008). When these data were unavailable (nine galaxies), we adopted the SFR(TIR) prescription by Murphy et al. (2011) using the fluxes by Engelbracht et al. (2008). For SBS 0335−052 and I Zw 18, we adopted the SFRs from radio free–free emission (Hunt et al. 2004; Hunt, Dyer & Thuan 2005; Johnson, Hunt & Reines 2009), given the superiority of such estimates over other methods (e.g. Murphy et al. 2011). For one galaxy in the starburst sample (UM 420), because of the lack of *Spitzer*/Multiband Imaging Photometer (MIPS) observations, the SFR was estimated from Hα luminosities, and for one galaxy (ESO 489−G56), there were no data available from which to infer SFR (so it was not considered further). For the (23) BCDs from Hunt et al. (2010), total Hα fluxes were taken from Gil de Paz et al. (2003), Rosa-González

Table 1. Characteristics of the individual samples in the MEGA data set.

Parent sample	Redshift range	Number	Selection criterion	Original O/H calibration	SF method	Reference
			Local Universe			
KINGFISH	−0.001–0.008	55	Representative	KK04	FUV+TIR[a]	Kennicutt et al. (2011)
LVL	−0.001–0.003	138	Volume-limited	M91, KK04, Direct[b]	FUV+TIR[a]	Kennicutt et al. (2008)
Starburst	0.0–0.058	41	Representative	Direct[c]	Hα+24 μm[d]	Engelbracht et al. (2008)
BCD	0.009–0.044	23	Primordial helium	Direct[c]	Hα+24 μm[d]	Hunt et al. (2010)
			$0.1 \leq z \lesssim 0.9$			
COSMOS	0.17–0.91	334	*I* band	KD02	Hα, Hβ	Cresci et al. (2012)
COSMOS	0.62–0.69	26	[O III] λλ4959, 5007	KK04	SED fitting	Henry et al. (2013)
DEEP2	0.71–0.91	27	[O III] λ4363	Direct	Hβ	Ly et al. (2015)
NewHα	0.79–0.82	143[e]	Narrow-band Hα	T04	Hα	de los Reyes et al. (2015)
HST-grism	0.60–2.32	11	[O III] λλ4959,5007, [O II] λ3727	KK04	Hβ	Xia et al. (2012)
			$z > 0.9$			
DEEP2	1.02–1.40	9	*R* band	PP04N2	Hα	Shapley et al. (2005)
DEEP2	1.02–1.40	7	*R* band	PP04N2	Hα	Liu et al. (2008)
VVDS	1.27–1.53	6	[O II] λ3727	T04	Hα	Queyrel et al. (2009)
BX	2.11–2.43	7	$U_n - G$, $G - \mathcal{R}$ colours	PP04N2	Hα	Shapley et al. (2004)
KBSS	2.02–2.55	79	*H* band[f]	PP04O3N2	Hα[g]	Steidel et al. (2014a)
LSD	2.93–3.41	8	Lyman-break dropout	KD02	Hα	Mannucci et al. (2009)
AMAZE	3.04–4.87	26	Lyman-break dropout	KD02	Hα	Troncoso et al. (2014)
COSMOS	2.97–3.69	35	Predicted Hβ	KD02	UV	Onodera et al. (2016)
			Stacked samples			
SXDS/UDS	1.27–1.52	5[h]	*K* band	PP04N2	Hα	Yabe et al. (2014)
COSMOS	1.40–1.70	10[h]	sBzK	PP04N2	Hα	Zahid et al. (2014)

[a]If not available, then SFR(FUV), or as last choice SFR(TIR).
[b]Taken from Berg et al. (2012) or Marble et al. (2010) when available, otherwise from Moustakas et al. (2010) (KK04).
[c]Taken from Berg et al. (2012), Guseva et al. (2003a,b, 2011, 2012), Izotov & Thuan (2004), Izotov et al. (2006, 2009), Izotov, Thuan & Stasińska (2007), Izotov, Thuan & Privon (2012), Kobulnicky & Skillman (1996, 1997), Kniazev et al. (2003, 2004), Mattsson, Pilyugin & Bergvall (2011), Pérez-Montero & Díaz (2005), Roennback & Bergvall (1995), Shi et al. (2005), Thuan & Izotov (2005), Vigroux, Stasińska & Comte (1987), and Zhao, Gao & Gu (2010).
[d]If not available, then the maximum of SFR(TIR) and SFR(Hα).
[e]AGN have been excluded.
[f]This is only one of several 'layered' criteria for selecting the galaxies for KBSS Keck-MOSFIRE observations.
[g]SFRs are taken from Steidel et al. (2014b).
[h]These are from stacked spectra, but are treated here as individual measurements; the redshifts are taken as the average given in the respective papers ($z \sim 1.4$ and $z \sim 1.6$ for Yabe et al. 2014; Zahid et al. 2014, respectively).

et al. (2007), Pérez-Montero et al. (2011), Lagos et al. (2014), and 24 μm fluxes from Hunt et al. (in preparation). As for the starbursts, for the three galaxies without Hα data, we used SFR(TIR), and for SBS 1030+583 there were no MIPS data so we adopted SFR(Hα).

Considering the different SFR estimators discussed above, and considering their varying degrees of applicability, for the local samples the uncertainties on the SFRs are probably around a factor of 2 (0.3 dex). As mentioned above, the SFRs have been reported to a Chabrier (2003) IMF.

2.1.2 *Stellar masses*

We calculated the stellar masses according to Wen et al. (2013), a method based on *WISE W*1 (3.4 μm) luminosities. This approach exploits the approximately constant mass-to-light ratios of stellar populations at near-infrared wavelengths, independently of metallicity and age (McGaugh & Schombert 2014; Norris et al. 2014). However, when *W*1 photometry was not available, we used *Spitzer*/Infrared Array Camera (IRAC) 3.6 μm photometry instead. In fact, the two bands are very similar; using data from Brown et al. (2014), Grossi et al. (2015) find for spirals a mean flux ratio $F_{3.4}/F_{3.6} = 1.02 \pm 0.035$. Including also the data for dwarf irregulars from Brown et al. (2014), we find a mean flux ratio $F_{3.4}/F_{3.6} = 0.98 \pm 0.061$. Thus, we conclude that the ratio of the *W*1 to IRAC 3.6 μm bands is unity, with 5–6 per cent scatter for galaxies like our targets.

For the starburst and BCD samples, we used the H II-galaxy formulation by Wen et al. (2013), rather than what they found for their full sample; the H II galaxies have the lowest mass-to-light ratios in their compilation, corresponding roughly to the bluest regions of the galaxies studied by Zibetti, Charlot & Rix (2009). To better take into account the weak trends with abundance found by Wen et al. (2013), we also applied an approximate correction for low metallicity (by multiplying the mass-to-light ratio by 0.8 when $12+\log(\mathrm{O/H}) \leq 8.2$; Wen et al. 2013, see their fig. 17). Instead, for the LVL and KINGFISH samples, we adopted the Wen et al. (2013) formulation based on morphological type, and considered an 'early-type' galaxy one with Hubble type $T < 2$.[2]

However, before applying the relations by Wen et al. (2013), we first subtracted nebular emission and emission from hot dust where possible. In starbursts and BCDs, such contamination can be very important in the near-infrared and can contribute 50 per cent

[2] The distinction used by Wen et al. (2013) is based on colours which are not available for all our samples.

or more to the observed flux at these wavelengths (Hunt, Vanzi & Thuan 2001; Hunt, Giovanardi & Helou 2002; Smith & Hancock 2009; Hunt et al. 2012). The ionized gas continuum contribution to the 3.4–3.6 μm flux was estimated from the SFR using the emission coefficients from Osterbrock & Ferland (2006). When possible, we also subtracted the hot-dust component, with the assumption that *H*-band emission is entirely stellar. Because *H*-band photometry is available for some of our sample, we used the data from Brown et al. (2014) to estimate the maximum possible IRAC 3.6 μm/*H*-band ratio in galaxies similar to our targets; 95 per cent of the spiral/dwarf irregular galaxies have a flux ratio ≤2.4. This corresponds to a (Vega-based) $[H-3.6]$ colour of ∼0.8, consistent with what is found for the pure stellar component in star-forming galaxies (Hunt et al. 2002). After subtraction of the nebular component, any excess over this ratio was attributed to hot dust and subtracted; this subtraction was not possible for 33 galaxies, including all the BCDs.

We compared the stellar masses obtained with the formulation of Wen et al. (2013) to those calculated according to Lee et al. (2006) based on IRAC 4.5 μm luminosities (used by Hunt et al. 2012). For the BCDs, the masses based on Wen et al. (2013) are on average −0.2 dex lower than those based on Lee et al. (2006) with a scatter of 0.15 dex; this is not unexpected given the blue colours of these galaxies and the results of Zibetti et al. (2009) who showed that the Bell & de Jong (2001) calibration used by Lee et al. (2006) gives mass-to-light ratios that are too high for such blue galaxies. Instead for the starbursts, the two estimates are in closer agreement, with −0.06 dex difference on average and a scatter of 0.20 dex. Moreover, for the galaxies having both *W*1 and IRAC data, the stellar masses obtained from 3.6 μm luminosities are within ∼5 per cent of those from *W*1 as expected.

For LVL, we have compared our estimates with those from Cook et al. (2014) who used a constant mass-to-light ratio and the IRAC 3.6 μm luminosity. The Wen-derived stellar masses are on average −0.25 dex smaller than the Cook et al. (2014) values, with a scatter of 0.09 dex. Skibba et al. (2011) derived stellar masses for the KINGFISH sample according to the formulation of Zibetti et al. (2009) based on optical and *H*-band colours. We have compared ours derived using Wen et al. (2013) to theirs and find that the values from Skibba et al. (2011) are smaller by ∼0.5 dex on average, with a 0.3 dex scatter.

Given the significant uncertainties inherent in the procedures to derive stellar masses over a wide range of galaxy types, and considering the offsets and scatters of our new M_* estimates, the uncertainties on the stellar masses for the local samples are at most a factor of 2 (0.3 dex). As above, these values are based on a Chabrier (2003) IMF.

2.2 SDSS10 $z \simeq 0$ galaxy sample

Mannucci et al. (2010) analysed a set of emission-line galaxies from the SDSS, using the stellar masses from Kauffmann et al. (2003), and SFRs measured from Hα after correcting for extinction using the Balmer decrement; they reported all values to a Chabrier (2003) IMF. The parameter range covered by this sample is much more limited than the MEGA sample: $9.2 \lesssim \mathrm{dex}(M_*) \lesssim 11.3$ $M_\odot$; $8.5 \lesssim 12+\log(\mathrm{O/H}) \lesssim 9.1$ [assuming the Kewley & Dopita (2002) calibration, see below]; $-1.3 \lesssim \log(\mathrm{SFR}) \lesssim 0.8$ $M_\odot$ yr^{-1}. Nevertheless, we include this sample, hereafter SDSS10, in our analysis because of its superb statistics for comparison both locally and at $z > 0$.

2.3 $z > 0$ samples

Because our analysis is focused on observationally constraining metal content at high redshift, to construct the MEGA data set we have culled from the literature all available samples at $z > 0$ with measured M_*, SFR, and O/H. Stacked analyses have been avoided where possible, and are used only to increase statistics when tabulations of observations for individual galaxies were not available in the required redshift range. We identified 14 samples at $z > 0.1$ (see Table 1) for which these three parameters were measured. Unavoidably, this compilation is subject to a variety of selection effects which change with sample and redshift. Nevertheless, from the observational point of view, the MEGA data set constitutes a unique tool with which to assess basic trends among M_*, SFR, and O/H, and establish how they vary with redshift. Table 1 lists the samples that comprise the MEGA data set, together with their redshift range, selection technique, and other information. We postpone the important discussion of metallicity estimates to Section 3.

2.3.1 $0.1 \leq z \leq 0.9$

The most important representative samples in the redshift range $0.1 \leq z \lesssim 0.9$ come from two surveys, zCOSMOS (Lilly et al. 2009; Cresci et al. 2012) and NewHα (de los Reyes et al. 2015); these two data sets alone comprise 477 galaxies. The first, from COSMOS, is *I* band selected and was first described by Lilly et al. (2009). Cresci et al. (2012) derived stellar masses from fitting spectral energy distributions (SEDs) of 12 photometric bands, including *Spitzer*/IRAC data at 3.6–5.8 μm. They calculated SFRs from Hα and Hβ luminosities, after correcting for extinction either via the Balmer decrement (for galaxies with $z \lesssim 0.49$) or using the extinction estimated from the SED fitting with an appropriate multiplicative factor. The second large sample in this redshift range comes from the New Hα survey, selected from narrow-band Hα images designed to identify emission-line galaxies around $z \approx 0.8$. de los Reyes et al. (2015) calculate stellar masses through SED fitting of eight photometric bands (up to observed frame *J* band), and estimate SFRs from the Hα images after correcting for the contribution from [N II] and for extinction.

Unlike Hunt et al. (2012), we do not include in the MEGA data set the luminous compact galaxies (LCGs) by Izotov, Guseva & Thuan (2011) and the 'Green Peas' (Amorín, Pérez-Montero & Vílchez 2010); the latter galaxies are selected by bright [O III] λ5007 emission in the SDSS *r* band (Cardamone et al. 2009). LCGs, instead, are defined by requiring an [O III] λ4363 detection, large Hβ equivalent width (EW), and a flux limit in Hβ. Thus, the LCGs are young (because of the high Hβ EW), highly star-forming (because of the Hβ flux limit) and metal-poor (because of the [O III] λ4363 detection). Although highly interesting objects, the Izotov et al. (2011) selection criteria favour young, metal-poor galaxies, and thus are not be representative of abundances of typical galaxy populations at those redshifts.

There are ∼60 galaxies in the remaining three samples in this redshift range: galaxies selected from a multi-slit narrow-band spectroscopic survey with [O III] λλ4959, 5007, [O II] λλ3727, 3729 at $z \sim 0.6$–0.7 by Henry et al. (2013); [O III] λ4363 DEEP2 selected objects at $z \sim 0.7$–0.9 by Ly et al. (2015); and galaxies selected from *HST*-grism observations ([O III], [O II]) by Xia et al. (2012). These three samples are very interesting because of their selection methods which tend to favour less massive galaxies than typical broad-band photometry selections. Stellar masses were derived from SED

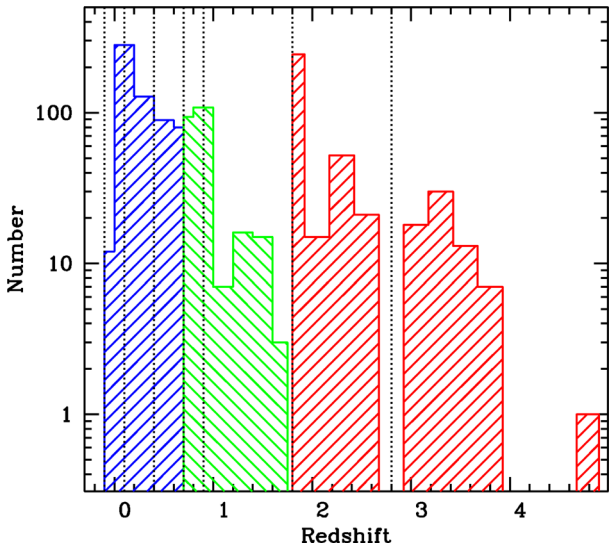

Figure 1. Redshift distribution of combined sample (without SDSS10). The seven redshift bins used throughout the paper for the MEGA data set are also shown as vertical dotted lines. The colours of the portions of the histogram are arbitrary, with the aim of illustrating 'low' redshift (blue), 'intermediate' redshifts (green), and 'high' redshifts (red).

fitting of COSMOS imaging data including IRAC bands (Henry et al. 2013), of 8-band photometry up to z' for the DEEP2 survey (Ly et al. 2015), and of 10-band *Hubble Space Telescope* (*HST*) ACS/WFC3 photometry up to $F160W$ (Xia et al. 2012). With the exception of Henry et al. (2013) who used SED fitting to calculate SFRs, Hα and Hβ corrected luminosities were used to infer SFRs.

2.3.2 $z > 0.9$

Most of the galaxies in this redshift range are colour-selected Lyman-break galaxies (e.g. Steidel et al. 1999). However, the Queyrel et al. (2009) galaxies are selected from the magnitude-limited Mass Assembly Survey with SINFONI in VVDS (MASSIV; Epinat et al. 2009), and the two $z \sim 1$ samples by Shapley et al. (2005) and Liu et al. (2008) are selected from the DEEP2 Galaxy Redshift Survey (Davis et al. 2003). Wavelength coverage for stellar-mass determinations varies, with $U_nG\mathcal{R}K_s$ (Shapley et al. 2004); $BRIK_s$ (Shapley et al. 2005; Liu et al. 2008); $UBVRIZ_sJK$ (Queyrel et al. 2009); and 14 spectral bands from GOODS-MUSIC (Grazian et al. 2006), including IRAC 3.6, 4.5 μm (Mannucci et al. 2009; Troncoso et al. 2014). Stellar masses for the Onodera et al. (2016) COSMOS sample are fitted with *uBVrizYJHK* and IRAC bands. Onodera et al. (2016) prefer SFRs inferred from extinction-corrected UV luminosities, but all other SFRs in this redshift range are determined from Hα suitably corrected for extinction.

To ensure better coverage of the redshift range $1.3 < z < 1.7$, we have included also the two samples by Yabe et al. (2014) and Zahid et al. (2014). Neither group publishes data for individual galaxies, so we have adopted the parameters of their stacked spectra here as individual galaxies, and used the average redshifts of $z \sim 1.4$ and $z \sim 1.6$ for Yabe et al. (2014) and Zahid et al. (2014), respectively.

The redshift distribution of the MEGA data set is shown in Fig. 1, together with the seven redshift bins that will be used throughout the paper. As mentioned above, Table 1 gives the characteristics of the 19 individual samples comprising the MEGA data set; there is a total of 990 galaxies from $z \simeq 0$ to $z \sim 3.7$ (and LnA1689−2 in the AMAZE sample at $z = 4.87$).

3 METALLICITY CALIBRATIONS

Oxygen abundance O/H is typically used as a proxy for metallicity in emission-line galaxies. Because the ionized gas in H II regions at lower metal abundance is hotter (as measured by electron temperature, T_e), the preferred technique to establish O/H is to measure T_e and the physical conditions in the ionized plasma. In this 'direct-temperature' or 'T_e' method, the T_e of the ionized gas is derived from the ratio of the [O III] λ4363 auroral line to lower excitation lines ([O III] λ4959, 5007); such flux ratios are sensitive to temperature because the auroral and strong lines originate from different excitation states (second and first excited states, respectively). Because the oxygen transitions are collisionally excited, the relative population of the excited states depends on T_e. Thus, the strengths of these forbidden lines, combined with the measurement of T_e and density in the nebula, can be converted to an abundance, relative to hydrogen, after correcting for unseen phases of ionization (e.g. Osterbrock & Ferland 2006).

Although the T_e method is more directly related to metallicity, the auroral lines are weak and often difficult to detect, especially at high metallicity. Thus, 'strong-line' methods are more generally used to estimate O/H, especially in metal-rich objects and at high redshift. It is necessary to calibrate these methods, either using theoretical photoionization models (e.g. Kewley & Dopita 2002, hereafter KD02) or measurements of T_e (e.g. Pettini & Pagel 2004, hereafter PP04), or a combination of the two (e.g. Denicoló, Terlevich & Terlevich 2002, hereafter D02). Despite the best efforts to correctly cross-calibrate these methods over a wide range of physical conditions, there remain large discrepancies, as high as 0.6 dex in log(O/H) (e.g. Kewley & Ellison 2008, and references therein). Thus to correctly assess metal content and its evolution with redshift, it is necessary to apply a common metallicity calibration to the samples under discussion.

In nearby galaxies where spectra can be obtained with sufficient signal-to-noise, the T_e method is generally used. As mentioned above, the most widely used auroral T_e diagnostic line is [O III] λ4363 because of its relative ease of observation, high abundance of emitting ions, and notable strength in the low- and intermediate-metallicity regime (i.e. below solar metallicity). However, there are several potential problems with the T_e method based on [O III].

(i) Metallicities derived from collisionally excited lines (CELs) such as [O III] can be underestimated when temperature fluctuations inside the nebula are present but neglected. The assumption of a single average CEL temperature for the whole nebula, usually higher than the temperature derived from the Balmer discontinuity, tends to lead to an underestimate of the abundances (e.g. Peimbert 1967; Stasińska 2005; Bresolin 2007; Pérez-Montero et al. 2010; Peña-Guerrero, Peimbert & Peimbert 2012).

(ii) Additional problems also plague the T_e method including possible non-Boltzmann electron distributions (e.g. Binette et al. 2012; Nicholls, Dopita & Sutherland 2012; Nicholls et al. 2013), depletion of oxygen on to dust grains (e.g. Peimbert & Peimbert 2010; Peña-Guerrero et al. 2012), and potential shock waves within the nebulae (e.g. Binette et al. 2012).

(iii) Finally, recent results suggest that metallicities derived from [O III] may be more unreliable than those from other auroral lines such as [S III] λ6312 and [N II] λ5755 (e.g. Berg et al. 2015);

however, these lines are even more difficult than [O III] to measure in distant galaxies.

An alternative to the use of T_e diagnostic lines can be the derivation of abundances from optical recombination lines (ORLs), because of their reduced emissivity dependence on density and temperature. Abundances derived from the ratio of the intensity of ORLs tend to be systematically higher than those from CELs (e.g. Peimbert, Storey & Torres-Peimbert 1993; Liu et al. 1995, 2001; Tsamis et al. 2004; García-Rojas & Esteban 2007). However, such differences may arise from the relation of the ORL abundances to small H-deficient portions of the regions, while the CEL-based metallicities are more representative of the whole nebula (see, e.g., Liu et al. 2000). Moreover, such lines are extremely faint, thus requiring very high signal-to-noise spectra that are currently available only for the Galaxy and the Local Group (e.g. Blanc et al. 2015).

There are also, perhaps more severe, problems with 'strong-line' methods, and the simplifying assumptions made for photoionization model calibrations (e.g. photoionization structure, geometry, stellar age; see Moustakas et al. 2010, for a thorough discussion). As for the T_e method, there may also be systematic discrepancies due to the metallicity-dependent correction for the depletion of oxygen on to dust grains (e.g. Peimbert & Peimbert 2010). Ultimately, the T_e method (with [O III]) is generally considered to be the most viable, given the limitations with other techniques.

Thus, to ensure the best possible comparison among different samples that rely on different O/H calibrations, it is advantageous to use the strong-line calibration method that most closely resembles values inferred from oxygen-based T_e-method estimations. According to the results of Andrews & Martini (2013), who used a stacking technique to measure the oxygen abundances of ∼200 000 star-forming galaxies from the SDSS to enhance the signal-to-noise ratio of the weak [O III] λ4363 line, there are three such methods: PP04 (both [N II] and [O III]+[N II]-based: hereafter PP04N2, PP04O3N2) and D02. Over the metallicity and M_* range covered by their calculations of various strong-line methods (see fig. 10 of Andrews & Martini 2013), the discrepancies between the T_e method and these three methods are $\lesssim$0.1 dex in 12+log(O/H).

Thus, in what follows, where there are no direct-T_e estimates, we have applied the transformations given by Kewley & Ellison (2008) to convert the original strong-line O/H calibrations for the MEGA data set (and SDSS10 sample) to the calibrations by D02 and PP04 (PP04N2, PP04O3N2). As reported in Table 1, the original O/H calibrations include KD02 (Kewley & Dopita 2002; Mannucci et al. 2010; Cresci et al. 2012; Troncoso et al. 2014); KK04 (Kobulnicky & Kewley 2004; Kennicutt et al. 2011; Xia et al. 2012; Henry et al. 2013); M91 (McGaugh 1991; Marble et al. 2010); PP04N2, PP04O3N2 (Pettini & Pagel 2004; Shapley et al. 2004, 2005; Liu et al. 2008; Yabe et al. 2012; Steidel et al. 2014a; Zahid et al. 2014); and T04 (Tremonti et al. 2004; de los Reyes et al. 2015).

4 SCALING RELATIONS AND THE FP

The MEGA data set comprises three parameters (pseudo-observables, as they are not directly observed): nebular oxygen abundance (12+log(O/H)), stellar mass (M_*), and SFR. As discussed in the introduction, these three parameters are mutually correlated, although O/H trends flatten at high M_* (and high O/H). Here we discuss the scaling relations of the three parameters: the mass–metallicity relation, MZR, the 'main sequence' of star formation, SFMS, and the correlation (at least at $z \sim 0$) between sSFR and metallicity.

The MZR with the PP04N2 O/H calibration for different redshift bins is shown in Fig. 2. The solid curve shows the T_e-method MZR derived by Andrews & Martini (2013) which well approximates the MEGA data set at $z \approx 0$. The dotted grey curves represent the polynomial fits given by Maiolino et al. (2008) for the KD02 calibration; at high M_*, these curves fail to capture the T_e-derived (or PP04N2) metallicities because of the different O/H calibration. As virtually all previous work suggests, the different panels illustrate that as z increases, at a given M_* metallicity decreases. However, at $z \approx 0$ for a given M_*, the starburst and BCD samples tend to be more metal-poor than the LVL and KINGFISH galaxies; they behave more like galaxies at $z \gtrsim 1$ than like galaxies in the Local Universe, presumably because of their higher sSFR.

The high sSFRs in the starburst and BCD $z \approx 0$ samples are more clearly seen in Fig. 3, which shows the SFMS, or sSFR plotted against M_*. The solid line shows the SFMS calibrated with the LVL+KINGFISH samples, having a slope of -0.19 ± 0.02, roughly consistent with that (-0.23) found by Elbaz et al. (2007) for $z \sim 0$ galaxies. The dashed grey lines correspond to the Speagle et al. (2014) formulation for SFR as a function of cosmic time (we have calculated cosmic age for representative redshifts and plotted the result). The slope by Speagle et al. (2014) at $z \gtrsim 2$ is similar to what we find for the Local Universe, which however is shallower (steeper in SFR–M_* space) than their value for $z \sim 0$. Fig. 3 illustrates that as redshift increases, for a given M_*, sSFR also increases; galaxies that would be main-sequence galaxies at $z \gtrsim 1$ are starbursts if found at $z \approx 0$. However, it is also seen from the figure that the individual high-z samples do not clearly follow the SFMS; this is almost certainly due to selection effects and will be further discussed in Section 5.2. Because of the difficulty in measuring metallicities in high-z emission-line galaxies, flux limits for spectroscopy impose a commensurate limit in SFRs.

The third correlation between sSFR and O/H is shown in Fig. 4. As in the previous figures, the solid line gives the local calibration on the LVL+KINGFISH and the dotted grey lines show the redshift trend for O/H expected for the higher SFR as predicted by the FPZ (see Section 4.2). The SFRs of the local starbursts and BCDs are higher at a given O/H, relative to the other local samples; again, they are more similar to galaxies at $z \gtrsim 1$ than to typical local populations. Similarly to the behaviour of the MEGA data set for the SFMS, the LVL+KINGFISH galaxies show a well-defined correlation between sSFR and O/H, but the correlation disappears for the higher redshift samples.

The main point of this third correlation is that, at least locally, the three psuedo-observables, 12+log(O/H), SFR, and M_*, are mutually interdependent. This makes it difficult to determine which is the primary parameter(s) driving the relations, and it is this point which we explore below in Section 4.2.

4.1 The SDSS10 relations

Similar correlations are found for the SDSS10 galaxies, although the range in M_*, O/H, and sSFR is smaller than in the MEGA data set. Nevertheless, over the limited parameter range the sheer number statistics afford precise determinations of scaling relations and fitting functions which will be important for constraining our models.

Fig. 5 gives the MZR for the three O/H calibrations of SDSS10 sample, transformed from the original KD02. The solid curves, also shown in Fig. 2, give the MZR for the direct-method O/H as found by Andrews & Martini (2013), while the dashed ones are functions

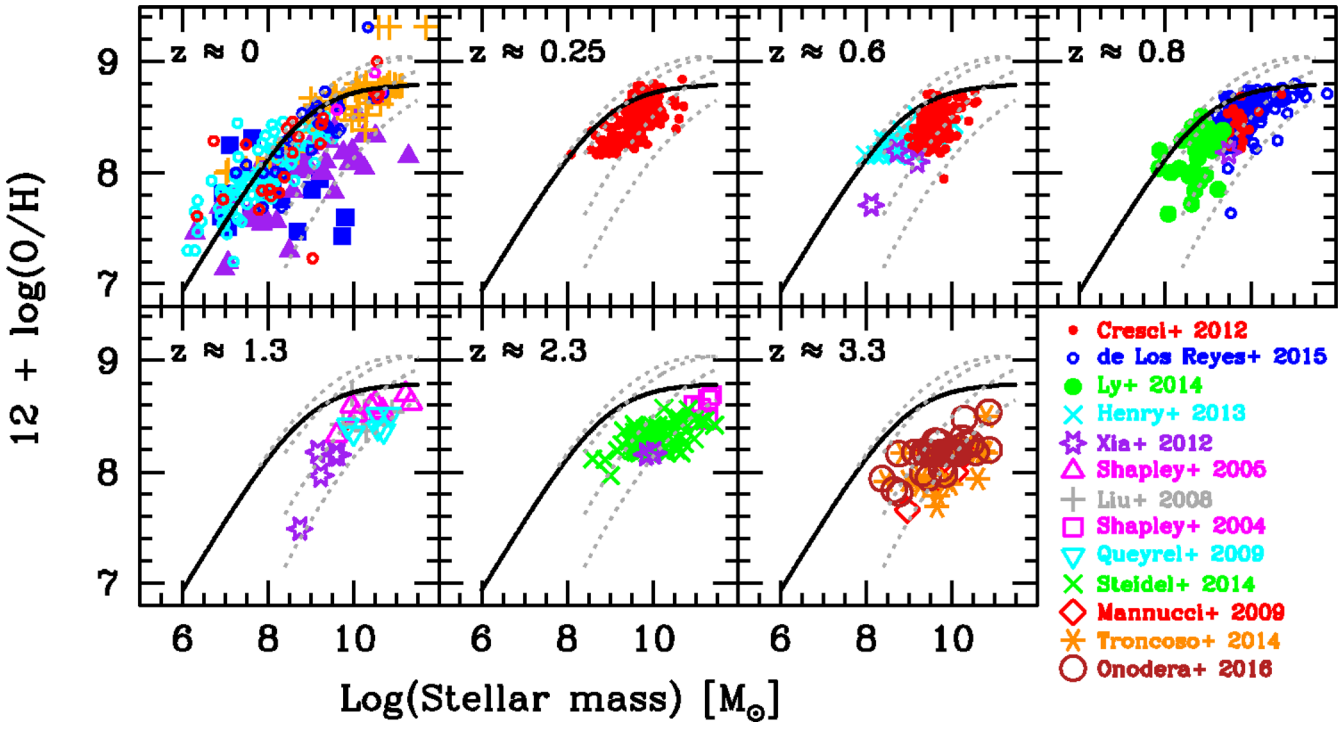

Figure 2. MZR over redshifts from $z \sim 0$ to $z \gtrsim 3.3$, binned as described in the text. The solid (black) curve (labelled $z \sim 0$) corresponds to the fit to SDSS10 (with stacked T_e metallicity determinations) by Andrews & Martini (2013), and the dotted (grey) curves to the polynomial fits by Maiolino et al. (2008) with the KD02 calibration at $z \approx 0.07$, $z \approx 0.7$, $z \approx 2.2$, and $z \approx 3.5$. The O/H calibration for all galaxies is PP04N2 as described in the text. Samples are labelled according to the legend in the lower rightmost panel, except for $z \approx 0$ which are as follows: LVL as small open circles (colours correspond to Hubble types with late types ($T \geq 8$) as cyan, $5 \leq T < 8$ as blue, $3 \leq T < 5$ as magenta, $T < 3$ as red); KINGFISH as (orange) pluses; Engelbracht et al. (2008) as (purple) filled triangles; Hunt et al. (2010) as (blue) filled squares. The stacked samples (Yabe et al. 2014; Zahid et al. 2014) at $z \approx 1$ are not plotted.

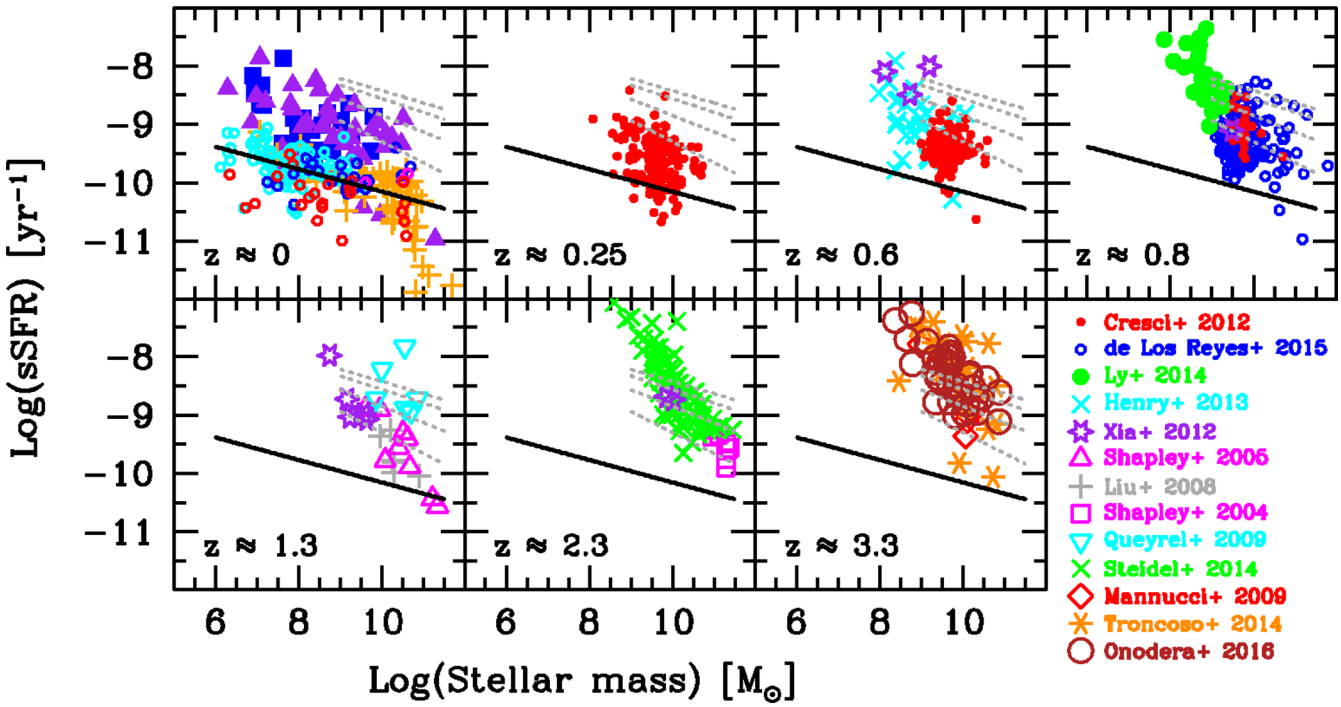

Figure 3. sSFR versus M_* (main sequence of SF) over redshifts from $z \sim 0$ to $z \gtrsim 3.3$, binned as described in the text. The solid (black) curve (labelled $z \sim 0$) corresponds to the fit to the LVL+KINGFISH samples, and the dotted (grey) curves to the formulation of dependence with M_* and z by Speagle et al. (2014) for $z \approx 0.6$, $z \approx 1.3$, $z \approx 2.3$, and $z \approx 3.3$. Symbols are as in Fig. 2, and the stacked samples (Yabe et al. 2014; Zahid et al. 2014) are not plotted.

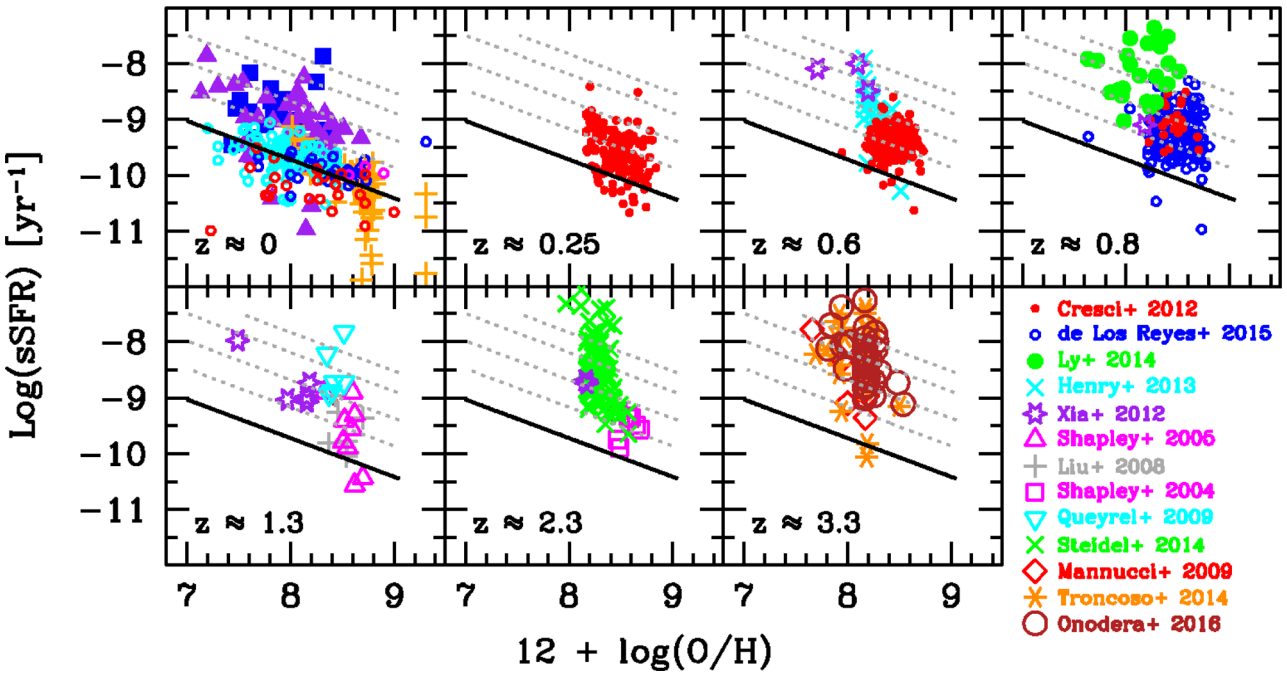

Figure 4. sSFR versus 12+log(O/H) over redshifts from $z \sim 0$ to $z \gtrsim 3.3$, binned as described in the text. The solid (black) line corresponds to the fit to the best-fitting slope for the MEGA sample at $z \sim 0$, and the dotted (grey) lines to the prediction of the redshift variation assuming the increase in sSFR given by Speagle et al. (2014, from $z \sim 0.6$, $z \sim 1.3$, $z \sim 2.3$, $z \sim 3.3$) of the FP for these two parameters described in Section 4.2. As in Fig. 2, the O/H calibration for all galaxies is PP04N2 as described in the text. Symbols are as in Fig. 2, and the stacked samples (Yabe et al. 2014; Zahid et al. 2014) are not plotted.

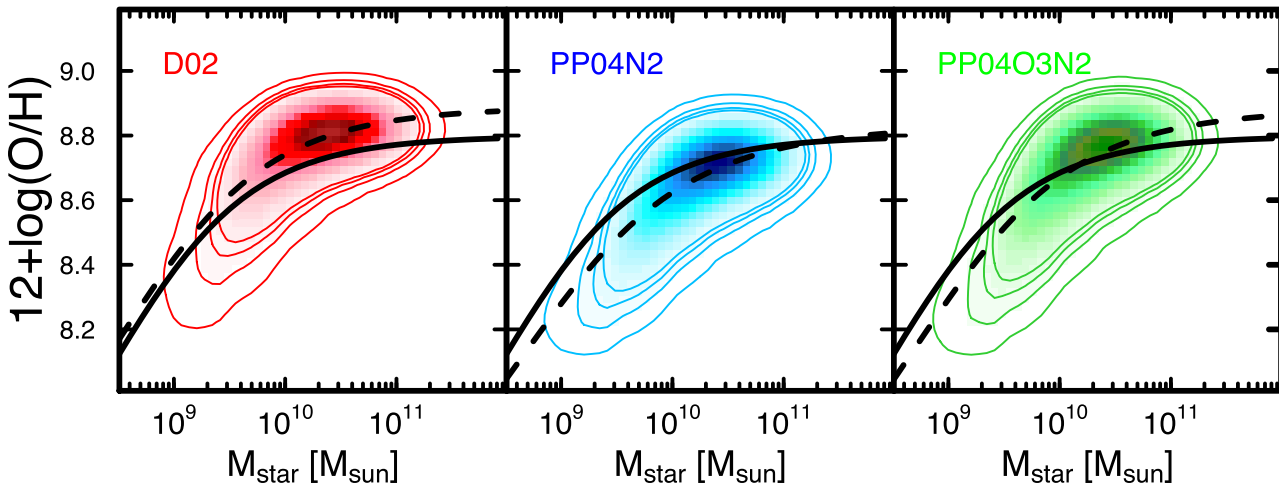

Figure 5. SDSS10 galaxies: 12+log(O/H) plotted against (log of) M_*. The three panels correspond to number densities of 12+log(O/H) (with the three O/H calibrations) and M_*. In each panel, the solid curves correspond to the MZR taken from Andrews & Martini (2013) for stacked O/H direct-temperature metallicity determinations as also shown in Fig. 2. The dashed curves show instead the relation of the form used by Andrews & Martini (2013) but fitted to the SDSS10 data used here.

of the same form but fitted to the SDSS10 data set itself. The PP04 calibrations (middle and right-hand panels) are, on average, the best approximation to the direct-method O/H curve, although at 12+log(O/H) $\lesssim$8.5, the D02 calibration is superior. In any case, the functional MZR form used by Andrews & Martini (2013) does not well approximate the SDSS10 data at low mass or low metallicities. The low-mass, low-metallicity linear portion of the data has a slope of $\sim 0.38 \pm 0.003$, similar to the MZR curve, but the latter is offset to higher masses.

The SFMS of the SDSS10 data is shown in Fig. 6; the solid line corresponds to the linear regression for the LVL+KINGFISH galaxies (also shown in Fig. 3) and the dashed curve to the Schechter-like functional form fitted by Salim et al. (2007). Although this last captures the low- and high-mass ends of the SDSS10 data, it does not pass through the region with the highest density (blue colours in Fig. 6). This could have something to do with the different ways that SFR is calculated; Salim et al. (2007) used FUV while Mannucci et al. (2010) used extinction-corrected Hα. Nevertheless, the

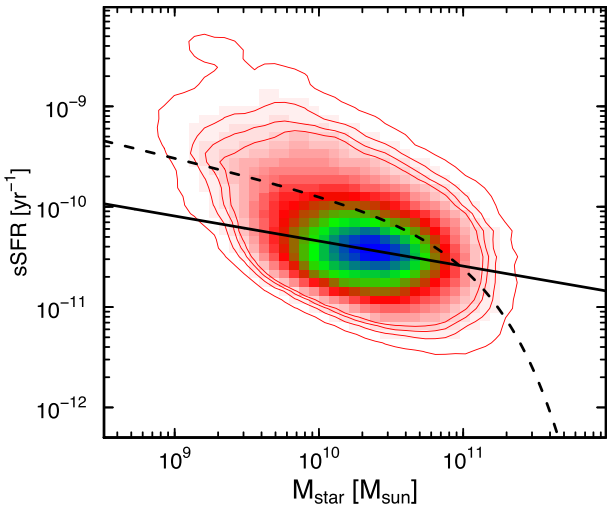

Figure 6. SDSS10 galaxies: sSFR plotted against M_*. The colour scale corresponds to the number densities of the two parameters. The solid curve gives the linear SF 'main-sequence' regression to the LVL+KINGFISH samples (also shown in Fig. 3), and the dashed curve to the Schechter function fitted by Salim et al. (2007).

LVL+KINGFISH regression well approximates this behaviour, implying that the SFR derivation is probably not the cause of the discrepancy. The third correlation, between sSFR and 12+log(O/H), is not shown for the SDSS10 data; it shows a similar behaviour to the MEGA sample.

4.2 A planar approximation to scaling relations

At high M_* and O/H, both the MZR and SFMS inflect and flatten (e.g. Tremonti et al. 2004; Noeske et al. 2007; Whitaker et al. 2014; Gavazzi et al. 2015; Lee et al. 2015). However, for M_* below a certain threshold, $M_* \leq 3 \times 10^{10}$ M$_\odot$, roughly the 'turn-over mass' (Tremonti et al. 2004; Wyder et al. 2007), the relations among the variables are approximately linear. We propose that, at high M_* and O/H, the inflections in the MZR and the SFMS compensate one another, and hypothesize that even above this inflection threshold, the trends in M_*, O/H, and SFR can be approximated by linear relations. Consequently, as discussed above, these observationally defined variables could define a *plane* which, given the relatively large scatters in the SFMS, the MZR, and the SFR–O/H relation, is not viewed in the best projection. Because the three parameters are mutually correlated, it is important to determine which of the three is the most fundamental, and whether or not the planar approximation is sufficient to describe the data. This can be readily accomplished through a PCA (e.g. Hunt et al. 2012).

The MEGA data set is a significant improvement on the sample studied by Hunt et al. (2012), and is particularly well suited for such an analysis. In particular, the MEGA data set triples the number of galaxies at $z \gtrsim 2-3$ with respect to Hunt et al. (2012). It spans almost two orders of magnitude in metallicity (12+log(O/H) = 7.1 to ∼9), a factor of ∼10^6 in SFR (∼$10^{-4} \leq$ SFR $\leq \sim 10^2$ M$_\odot$ yr^{-1}), and a factor of ∼10^5 in stellar mass (∼$10^6 \leq M_* \leq \sim 10^{11}$ M$_\odot$); moreover it includes galaxies at redshifts from $z \sim$ 0–3.8 (see Fig. 1). Other samples previously analysed to find scaling relations cover much smaller parameter ranges: typically less than a decade in metallicity (12+log(O/H) ≥ 8.4), a factor of ∼200 in SFR (∼0.04 $\lesssim$ SFR $\lesssim$ 6 M$_\odot$ yr^{-1}), and roughly two orders of magnitude in stellar mass ($M_* \gtrsim 10^9$ M$_\odot$; e.g. Tremonti et al. 2004; Lara-López et al. 2010; Mannucci et al. 2010; Yates, Kauffmann & Guo 2012). Because more than 50 per cent of the MEGA data set has $z > 0.5$, and it includes galaxies at redshift $z \gtrsim 3.5$, we can test the assumption that the relations among the observationally defined variables are redshift invariant.

4.3 PCA of the MEGA and SDSS10 samples

We have therefore performed a PCA for all three O/H calibrations of the MEGA data set without imposing a limit in M_* (cf. Hunt et al. 2012). A PCA diagonalizes the 3D covariance matrix, thus defining the orientation of the parameter space which minimizes the covariance. The orientation is contained in the eigenvectors which are, by definition, mutually orthogonal. If the 3D space formed by the three psuedo-observables is truly planar, we would expect most of the variance to be contained in the first two eigenvectors (the orientation of the plane); for the third eigenvector, perpendicular to the plane, the variance should be very small.

Independently of the O/H calibration, the PCA shows that the set of three observables truly defines a plane; $\gtrsim$98 per cent of the total variance is contained in the first two eigenvectors. Most (87 per cent) of the variance is contained in the first eigenvector alone (or principal component, PC), PC1; it is dominated by SFR, with M_* contributing slightly less, and O/H giving only a marginal contribution. PC2, the second eigenvector, holds 10–11 per cent of the variance, and is dominated by M_*, followed by SFR, and as in PC1, with O/H again only marginal. The smallest fraction of the variance (∼1.5–1.8 per cent) is contained in the third eigenvector, PC3, which is dominated by O/H; the implication is that O/H is the most *dependent* parameter, governed almost completely by M_* and SFR. Moreover, this means that the 3D space defined by O/H, SFR, and M_* is degenerate; because of the mutual correlations of the psuedo-observables, only two parameters are required to describe the properties of the galaxies.

We have also performed a PCA of the SDSS10 galaxies, and obtained similar results: namely the third eigenvector, PC3, the one dominated by O/H, contains the smallest fraction of the variance. The residuals of 0.05–0.06 dex are comparable to that obtained by the FMR formulation by Mannucci et al. (2010).

That star-forming galaxies form a plane in O/H, SFR, and M_* is not a new result. Lara-López et al. (2010) concluded that the 3D space of O/H, SFR, and M_* of ∼ 33 000 SDSS galaxies could be represented as a plane but used a regression analysis rather than a PCA (although see Lara-López, López-Sánchez & Hopkins 2013). Hunt et al. (2012) derived a PCA for a data set similar to ours, although dominated by LCGs, and also concluded that a 2D plane was sufficient to describe the 3D data set.

As in the introduction, we will refer to the resulting 2D plane as the FPZ. The FPZ for the MEGA data set is shown in the top panel of Fig. 7 where we have plotted 12+log(O/H) versus the equation that results from equating PC3 (PP04N2) to zero (see Table 2 for the other O/H calibrations):

$$12 + \log(\mathrm{O/H}) = -0.14 \log(\mathrm{SFR}) + 0.37 \log(M_*) + 4.82. \quad (1)$$

The bottom panel of Fig. 7 shows the residuals from the FPZ for the different O/H calibrations. For PP04N2, they are well approximated by a Gaussian with a $\sigma = 0.16$, corresponding to $\lesssim$45 per cent uncertainty; the other two O/H calibrations (D02, PP04O3N2) give similar results, although slightly larger (see Table 2). The residuals of the FPZ relation are independent of redshift to within 0.16 dex, the overall uncertainty; nevertheless the different symbols plotted

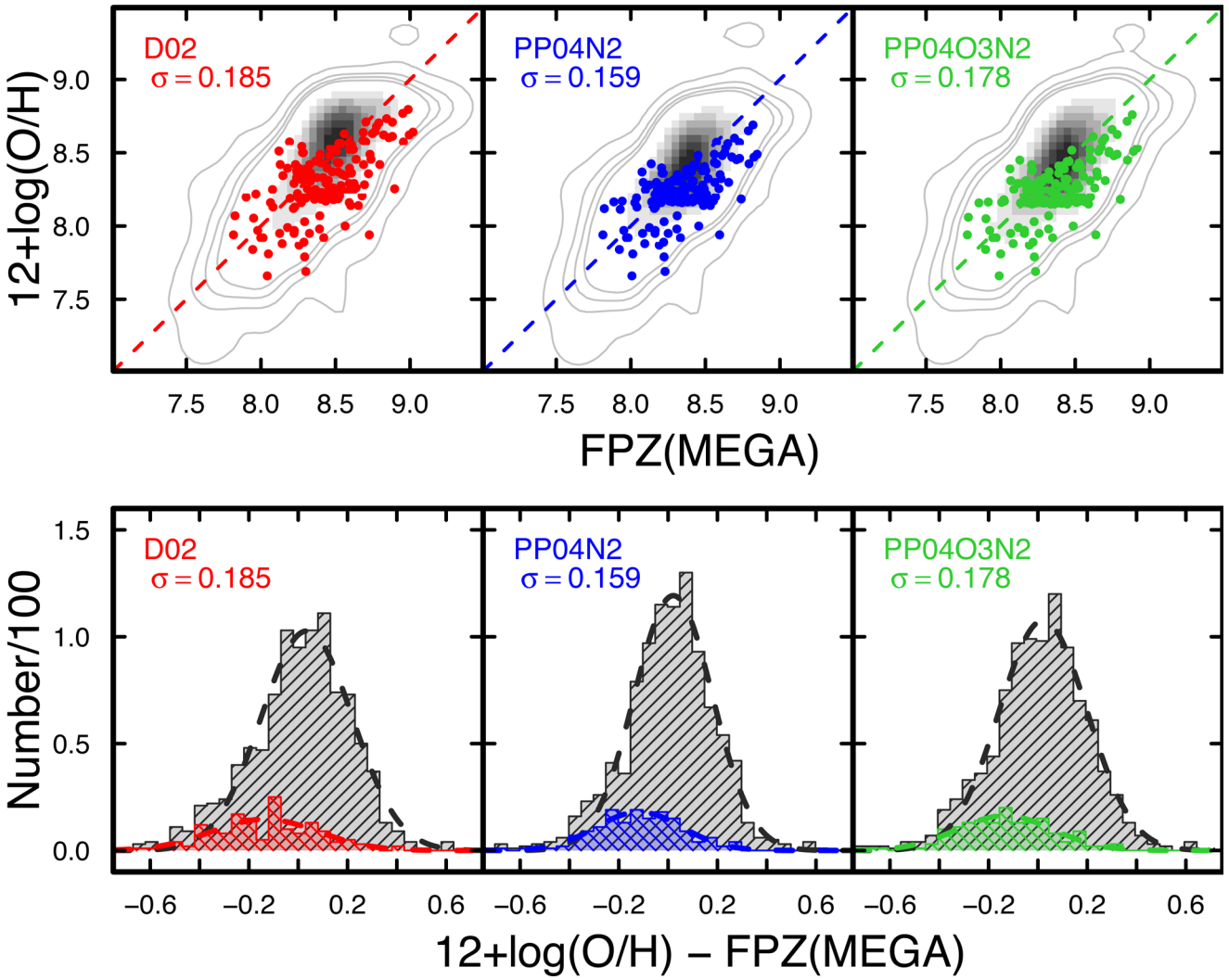

Figure 7. Top panel: FPZ projection of O/H for all O/H calibrations of the MEGA data set as described in the text. All galaxies are shown (in grey intensity and contours), including those with $M_* \geq 3 \times 10^{10}$ M$_\odot$; coloured filled circles correspond to galaxies with $z \geq 2$. The dashed lines give the identity relation. Bottom panel: histograms of FPZ residuals from the identity relation. The grey histograms show all galaxies, while the (lower amplitude) coloured ones correspond to galaxies with $z \geq 2$. The heavy dashed lines give the Gaussian fit of the residuals (including the separate fit to the galaxies with $z \geq 2$); the σ values in the upper-left corner of each panel correspond to the mean residuals for all galaxies. The width of the best (PP04N2) residual distribution over all redshifts is ∼0.16 dex (see the middle panels).

in the top panel (and the different histograms in the bottom one) suggest some slight deviation with redshift which we will explore in Section 5.3.

Because of the turnover of the MZR and SFMS at high stellar masses, our assumption of linearity in the FPZ could also produce a residual correlation with M_*. We have investigated this possibility and found that the FPZ residuals and (log)M_* are uncorrelated; the mean residuals of the regression are ∼0.16 dex (for the PP04 calibration), the same as those of the FPZ itself. Moreover, the slope of the FPZ residuals versus (log)M_* is zero to within the uncertainties (-0.015 ± 0.01). Thus, our hypothesis that the inflections in the MZR and SFMS compensate one another is apparently justified; the curvature in the MZR can be adequately accommodated by the increasing SFRs at high M_*, at least to within the uncertainties of our data.

The FPZ dispersion of ∼0.16–0.18 dex for the MEGA data set is higher than that found by Tremonti et al. (2004) for the MZR defined by 53 000 galaxies from the SDSS (0.1 dex), and also higher than the FMR (0.06 dex) found for the SDSS10 sample by Mannucci et al. (2010). However, as shown in Table 2, the SDSS10 data span limited ranges in O/H, SFR, stellar mass (and redshift) relative to the parameter space covered by the MEGA data. The mean and standard deviation of (log) stellar mass for the SDSS10 sample are 10.26 ± 0.41 M$_\odot$, while the comparable mean and standard deviation for MEGA are 9.44 ± 0.93 M$_\odot$; (log) SFR shows a similar pattern: -0.04 ± 0.43 M$_\odot$ yr^{-1} for SDSS10 compared to 0.16 ± 1.12 M$_\odot$ yr^{-1} for MEGA. Thus, the higher dispersion in the MEGA FPZ is not surprising despite the many more galaxies in SDSS.

The value of the FPZ dispersion is *lower* than the scatter of the MZR for ∼20 000 VVDS galaxies within individual redshift bins from $z \sim 0.3$–0.9 (∼0.20 dex; Lamareille et al. 2009). The FPZ dispersion for the ∼1000 galaxies studied here is only slightly higher than that found for the MZR of 25 nearby dwarf galaxies (0.12 dex; Lee et al. 2006), a sample dominated by low-mass galaxies. It is also only slightly higher than the rms scatter of 0.12 dex found by

Table 2. FPZ and FMR applied to MEGA and SDSS data sets[a].

Sample	Calibration	$\sigma_{\rm fit}^{b}$	Offset(fit)[b]	⟨12+log(O/H)⟩[c]	⟨log(SFR)⟩[c]	⟨log(M_*)⟩[c]	12+log(O/H) =	
(1)	(2)	(3)	(4)	(5)	(6)	(7)	(8)	
MEGA FPZ applied to the MEGA and SDSS10 data sets								
MEGA	D02	0.185	0.03	8.422 ± 0.33	0.159 ± 1.12	9.440 ± 0.93	$-0.17\,s + 0.44\,m + 4.33$	
MEGA	PP04N2	0.159	0.02	8.332 ± 0.30	0.159 ± 1.12	9.440 ± 0.93	$-0.14\,s + 0.37\,m + 4.82$	
MEGA	PP04O3N2	0.178	0.03	8.355 ± 0.32	0.159 ± 1.12	9.440 ± 0.93	$-0.16\,s + 0.41\,m + 4.48$	
SDSS10	D02	0.102	−0.04	8.768 ± 0.09	−0.038 ± 0.43	10.263 ± 0.41	As above for D02	
SDSS10	PP04N2	0.080	−0.004	8.660 ± 0.11	−0.038 ± 0.43	10.263 ± 0.41	As above for PP04N2	
SDSS10	PP04O3N2	0.088	−0.01	8.709 ± 0.12	−0.038 ± 0.43	10.263 ± 0.41	As above for PP04O3N2	
FMR[d] applied to the MEGA and SDSS10 data sets								
							12+log(O/H) =	
							$\mu_{0.32}$ <9.5 $M_\odot$[e]	$\mu_{0.32}$ ≥9.5 $M_\odot$[e]
(1)	(2)	(3)	(4)	(5)	(6)	(7)	(8)	(9)
MEGA	D02	0.175	−0.14	8.422 ± 0.33	0.159 ± 1.12	9.440 ± 0.93	$-0.16\,s + 0.51\,m + 3.83$	$-13.8 + 4.17m - 1.34\,s + 0.12m\,s - 0.19m^2 - 0.054s^2$
MEGA	PP04N2	0.168	−0.25	8.332 ± 0.30	0.159 ± 1.12	9.440 ± 0.93	$-0.16\,s + 0.51\,m + 3.83$	$-13.8 + 4.17m - 1.34\,s + 0.12m\,s - 0.19m^2 - 0.054s^2$
MEGA	PP04O3N2	0.181	−0.22	8.355 ± 0.32	0.159 ± 1.12	9.440 ± 0.93	$-0.16\,s + 0.51\,m + 3.83$	$-13.8 + 4.17m - 1.34\,s + 0.12m\,s - 0.19m^2 - 0.054s^2$
							12+log(O/H) =	
							$\mu_{0.32}$ <10.2 $M_\odot$[e]	$\mu_{0.32}$ >10.5 $M_\odot$[e]
(1)	(2)	(3)	(4)	(5)	(6)	(7)	(8)	(9)
SDSS10	D02	0.05	−0.25	8.768 ± 0.09	−0.038 ± 0.43	10.263 ± 0.41	$-0.15\,s + 0.47\,m + 4.20$	9.07
SDSS10	PP04N2	0.05	−0.34	8.660 ± 0.11	−0.038 ± 0.43	10.263 ± 0.41	$-0.15\,s + 0.47\,m + 4.20$	9.07
SDSS10	PP04O3N2	0.06	−0.28	8.709 ± 0.12	−0.038 ± 0.43	10.263 ± 0.41	$-0.15\,s + 0.47\,m + 4.20$	9.07

[a] Applying the FPZ and the FMR to the entire mass range according to equation (1). In the equations of columns 8 and 9, s corresponds to log(SFR) and m to log(M_*). The sense of the residuals is 12+log(O/H)(data) − 12+log(O/H)(FPZ,FMR).

[b] Standard deviation σ and offset of the FPZ or FMR residuals (e.g. Fig. 7).

[c] Means and standard deviations of the samples.

[d] We took the FMR for the MEGA sample from the extension to lower M_* by Mannucci et al. (2011), and for SDSS10 from Mannucci et al. (2010); for both we have converted their recipes with $\mu_{0.32}$ to the multiplicative formulation as for the FPZ.

[e] The divisions for the FMR are in $\mu_{0.32}$, where $\mu_{0.32} \equiv \log(M_*) - 0.32\,\log(\mathrm{SFR})$ (Mannucci et al. 2010).

Henry et al. (2013) for 18 galaxies at $z \sim 0.6$ in the mass range dex(8.5) $\leq M_* \leq$ dex(9.0). Because the dispersion in the MZR is found to increase with decreasing M_* (Tremonti et al. 2004; Mannucci, Salvaterra & Campisi 2011), a σ of 0.16 dex is a reasonable value, given the broad parameter space covered by our data set.

4.4 Comparison with the FMR

Table 2 gives the mean residuals and offsets of the FPZ applied to the MEGA and SDSS10 data sets, as well as of the FMR from Mannucci et al. (2010) applied to SDSS10, and the FMR extended to lower M_* by Mannucci et al. (2011) applied to the MEGA data set. Despite the vastly different parameter ranges over which the FPZ and FMR are calibrated, results from the table show that the FPZ and the FMR are roughly equivalent in terms of the width of the residuals, i.e. the accuracy of the approximation. The FPZ fits the SDSS10 data set almost as well as the FMR itself ($\sigma \approx 0.08$ dex), and the FMR is reasonably good at reproducing the metallicities of the MEGA data set.

However, the salient difference between the FPZ and FMR formulations is the negative O/H offsets of the FMR; column 4 of Table 2 shows that the FMR predicts metallicities both for the MEGA data set and for the recalibrated SDSS10 that can be in excess by as much as $\sim$−0.3 dex. A similar result was found by Hunt et al. (2012) relative to the FMR, although the offset was larger, $\sim$−0.4 dex, presumably because of the original SDSS10 KD02 calibration.

Indeed, the overlarge metallicities predicted by the FMR are almost certainly due to the different O/H calibrations as discussed in Section 3. Cullen et al. (2014) found a similar discrepancy of their observations at $z \sim 2$ with respect to the FMR using the same (KD02) calibration as Mannucci et al. (2010). Some groups concluded that the FMR evolves with redshift because of its failure to fit galaxies at $z \sim 2$–3 (e.g. Steidel et al. 2014a; Troncoso et al. 2014). However, we find that the FPZ, unlike the FMR, is apparently invariant with redshift; our result almost certainly stems from the common O/H calibration and its similarity to the T_e method by which strong-line methods are calibrated at low metallicity. Thus, it is of extreme importance to compare galaxies at different redshifts with a common O/H calibration that is as accurate as possible at low metallicities, and that smoothly connects these with the difficult intermediate-metallicity regime and with higher metallicities nearer to or exceeding solar.

5 METALLICITY AND SFR COEVOLUTION

Much work has been done to establish how metal abundance and SFR vary with redshift. As mentioned in the introduction, the picture that emerges from these studies is that the shape of the MZR is relatively invariant while the metallicity for a given M_* decreases with increasing redshift (e.g. Shapley et al. 2005; Erb et al. 2006a; Cowie & Barger 2008; Maiolino et al. 2008; Mannucci et al. 2009; Zahid et al. 2012; Henry et al. 2013; Steidel et al. 2014a; Troncoso et al. 2014; Yabe et al. 2014; Onodera et al. 2016). At the same time, it is well known that the SFMS also remains relatively constant in shape, but at a given M_*, SFR (and sSFR) increases with redshift (e.g. Noeske et al. 2007; Karim et al. 2011; Speagle et al. 2014). In the context of the FPZ, the relatively small dispersion of the residuals suggests that the FPZ formulation is apparently invariant with redshift to $z \sim$3.7, even with the new MEGA sample that more than triples the number of galaxies at $z \gtrsim 2-3$ with respect to Hunt et al. (2012). Thus, under the hypothesis that the FPZ is maintained even at high z, the opposing redshift trends of O/H and SFR must somehow be mutually compensated. For typical galaxy populations, at fixed M_*, the increase of SFR with redshift must be accompanied by a corresponding decrease in O/H. We can quantify such trends with the MEGA data set and the FPZ. Table 3 reports the median values of M_*, 12+log(O/H), and sSFR for the MEGA data set for six mass bins within the seven redshift bins shown in Fig. 1.

5.1 Redshift variation of O/H and sSFR

The trends with redshift of the MEGA data set are shown in Fig. 8 where 12+log(O/H) and sSFR are plotted versus redshift z. Following Karim et al. (2011), we have fitted the redshift variation with separable functions in M_* and z:

$$\mathrm{sSFR,\ O/H}(M_*, z) \propto M_*^{\beta}\ (1+z)^n.$$

The dependence on stellar mass is encompassed in the power-law index β, and the z dependence in the power-law index (slope in log space), n. The symbols in Fig. 8 correspond to data binned in redshift and in stellar mass as given in the legend (see Fig. 1 for redshift intervals); the error bars give the 25 per cent quantiles of the data within each bin.

For the trend of sSFR $\propto (1+z)^{n(\mathrm{sSFR})}$, the mean power-law index, $\langle n\rangle$(sSFR), averaged over all mass bins (except the lowest one, because of the lack of low-mass galaxies at $z \gtrsim 1$) is $\langle n\rangle(\mathrm{sSFR}) = 2.8 \pm 0.5$. For the M_* bins between dex(8.5) and dex(10) $\mathrm{M}_\odot$, n is relatively constant: 3.1 ± 0.37. This value is roughly consistent with n(sSFR) $\sim$ 3.4–3.5 to $z \sim 2$ as reported by Oliver et al. (2010) and Karim et al. (2011). For larger M_* ($M_* \geq 10^{10}\ \mathrm{M}_\odot$), the index decreases to $n(\mathrm{sSFR}) = 2.2$–2.4. Similar slopes and such a flattening are also seen in the highly star-forming sub-sample of COSMOS galaxies described by Karim et al. (2011); the MEGA data set probably represents a similarly highly star-forming sample, at least at the higher redshifts.

The redshift variation of O/H is represented by the mean power-law index $\langle n\rangle$(O/H), averaged over all mass bins (except the lowest one as above): $\langle n\rangle(\mathrm{O/H}) = -0.57 \pm 0.17$ for 12+log(O/H) $\propto (1+z)^{n(\mathrm{O/H})}$ (left-hand panel of Fig. 8). From the relatively small standard deviation, and visually evident in Fig. 8, it is apparent that the index n(O/H) is much more constant over variations in M_* than the equivalent index n(sSFR) for sSFR. Table 4 gives the fitted coefficients for the (PP04N2) metallicity redshift variation of the MEGA data set; these are the equations describing the dashed curves in the left-hand panel of Fig. 8 and subsequent figures.

5.2 Variation of O/H and sSFR with stellar mass

We now examine the M_* dependence of the redshift variations of O/H and sSFR. Fig. 9 shows 12+log(O/H) versus M_* (left-hand panel) and sSFR versus M_* (right), binned into different redshift bins; these are equivalent to the changes with redshift of the MZR (left-hand panel) and the SFMS (right).

Here we assess β in the separated formalism as above: sSFR, O/H $\propto M_*^{\beta}\ (1+z)^n$. β(O/H) corresponds roughly to the slope (power-law index) of the MZR, and β(sSFR) to the slope of the SFMS. For the M_* trend of O/H, $\langle\beta\rangle$ (averaged over all mass bins) is $\langle\beta\rangle(\mathrm{O/H}) = 0.21 \pm 0.05$. Both the normalization and the slope of the MZR are rather constant up to $z \sim 2$: $\beta = 0.24 \pm 0.03$, 12+log(O/H)(M_* = dex(9) $\mathrm{M}_\odot$) = 8.28 ± 0.04 (averages and standard deviations over five equally weighted redshift bins for $z < 1.8$). However, for $z > 2$, both the normalization and the slope gradually decrease: $\beta = 0.15 \pm 0.03$ and

Table 3. Median stellar masses, (PP04N2) O/H, and sSFR in MEGA redshift bins[a].

Redshift bin	Mass bin	Number	$\log(M_*)$ ($M_\odot$)	12+log(O/H) (PP04N2)	log(sSFR) ($M_\odot$ yr^{-1})
$z \leq 0.1$	$\log(M_*) < 8.5$	128	$7.76^{+0.31}_{-0.58}$	$7.92^{+0.12}_{-0.22}$	$-9.61^{+0.28}_{-0.23}$
	$8.5 \leq \log(M_*) < 9$	24	$8.69^{+0.11}_{-0.09}$	$8.16^{+0.10}_{-0.10}$	$-9.78^{+0.60}_{-0.18}$
	$9 \leq \log(M_*) < 9.5$	34	$9.18^{+0.12}_{-0.11}$	$8.39^{+0.09}_{-0.13}$	$-9.84^{+0.46}_{-0.18}$
	$9.5 \leq \log(M_*) < 10$	18	$9.64^{+0.15}_{-0.05}$	$8.39^{+0.19}_{-0.21}$	$-9.94^{+0.30}_{-0.11}$
	$10 \leq \log(M_*) < 10.5$	26	$10.28^{+0.12}_{-0.13}$	$8.69^{+0.08}_{-0.14}$	$-9.99^{+0.16}_{-0.15}$
	$\log(M_*) > 10.5$	27	$10.71^{+0.12}_{-0.11}$	$8.75^{+0.04}_{-0.03}$	$-10.36^{+0.30}_{-0.62}$
$0.1 < z \leq 0.4$	$\log(M_*) < 8.5$	1	8.09	8.16	−8.91
	$8.5 \leq \log(M_*) < 9$	16	$8.83^{+0.08}_{-0.16}$	$8.22^{+0.08}_{-0.04}$	$-9.22^{+0.11}_{-0.32}$
	$9 \leq \log(M_*) < 9.5$	39	$9.35^{+0.09}_{-0.23}$	$8.34^{+0.10}_{-0.07}$	$-9.52^{+0.27}_{-0.33}$
	$9.5 \leq \log(M_*) < 10$	84	$9.71^{+0.12}_{-0.11}$	$8.53^{+0.11}_{-0.10}$	$-9.69^{+0.30}_{-0.24}$
	$10 \leq \log(M_*) < 10.5$	18	$10.11^{+0.09}_{-0.05}$	$8.62^{+0.06}_{-0.11}$	$-9.78^{+0.25}_{-0.24}$
	$\log(M_*) > 10.5$	6	$10.57^{+0.10}_{-0.04}$	$8.60^{+0.04}_{-0.09}$	$-9.72^{+0.08}_{-0.05}$
$0.4 < z \leq 0.7$	$\log(M_*) < 8.5$	9	$8.38^{+0.02}_{-0.16}$	$8.19^{+0.04}_{-0.03}$	$-8.58^{+0.30}_{-0.36}$
	$8.5 \leq \log(M_*) < 9$	12	$8.82^{+0.15}_{-0.13}$	$8.25^{+0.05}_{-0.05}$	$-9.02^{+0.36}_{-0.17}$
	$9 \leq \log(M_*) < 9.5$	49	$9.34^{+0.09}_{-0.07}$	$8.35^{+0.13}_{-0.07}$	$-9.45^{+0.25}_{-0.14}$
	$9.5 \leq \log(M_*) < 10$	84	$9.69^{+0.09}_{-0.08}$	$8.44^{+0.09}_{-0.08}$	$-9.41^{+0.18}_{-0.21}$
	$10 \leq \log(M_*) < 10.5$	12	$10.12^{+0.10}_{-0.04}$	$8.59^{+0.02}_{-0.11}$	$-9.37^{+0.22}_{-0.12}$
	$\log(M_*) > 10.5$	3	$10.53^{+0.03}_{-0.00}$	$8.64^{+0.05}_{-0.01}$	$-9.57^{+0.15}_{-0.05}$
$0.7 < z \leq 0.9$	$\log(M_*) < 8.5$	6	$8.10^{+0.18}_{-0.18}$	$8.04^{+0.12}_{-0.03}$	$-7.58^{+0.46}_{-0.26}$
	$8.5 \leq \log(M_*) < 9$	16	$8.73^{+0.12}_{-0.05}$	$8.17^{+0.18}_{-0.20}$	$-8.07^{+0.39}_{-0.38}$
	$9 \leq \log(M_*) < 9.5$	45	$9.34^{+0.11}_{-0.07}$	$8.33^{+0.11}_{-0.07}$	$-9.13^{+0.43}_{-0.28}$
	$9.5 \leq \log(M_*) < 10$	91	$9.73^{+0.08}_{-0.11}$	$8.44^{+0.11}_{-0.09}$	$-9.21^{+0.27}_{-0.29}$
	$10 \leq \log(M_*) < 10.5$	22	$10.21^{+0.08}_{-0.12}$	$8.60^{+0.07}_{-0.08}$	$-9.23^{+0.27}_{-0.24}$
	$\log(M_*) > 10.5$	20	$10.74^{+0.24}_{-0.08}$	$8.69^{+0.04}_{-0.05}$	$-9.54^{+0.34}_{-0.26}$
$0.9 < z \leq 1.8$	$\log(M_*) < 8.5$	0	–	–	–
	$8.5 \leq \log(M_*) < 9$	1	8.74	7.49	−7.98
	$9 \leq \log(M_*) < 9.5$	2	$9.20^{+0.02}_{-0.02}$	$8.08^{+0.05}_{-0.05}$	$-8.88^{+0.08}_{-0.08}$
	$9.5 \leq \log(M_*) < 10$	14	$9.81^{+0.11}_{-0.17}$	$8.41^{+0.04}_{-0.06}$	$-8.81^{+0.28}_{-0.17}$
	$10 \leq \log(M_*) < 10.5$	14	$10.24^{+0.05}_{-0.11}$	$8.52^{+0.02}_{-0.03}$	$-8.67^{+0.06}_{-1.06}$
	$\log(M_*) > 10.5$	12	$10.68^{+0.17}_{-0.13}$	$8.54^{+0.07}_{-0.03}$	$-9.12^{+0.31}_{-0.81}$
$1.8 < z \leq 2.8$	$\log(M_*) < 8.5$	0	–	–	–
	$8.5 \leq \log(M_*) < 9$	2	$8.74^{+0.07}_{-0.07}$	$8.12^{+0.01}_{-0.01}$	$-7.22^{+0.07}_{-0.07}$
	$9 \leq \log(M_*) < 9.5$	5	$9.28^{+0.03}_{-0.10}$	$8.25^{+0.03}_{-0.05}$	$-7.69^{+0.05}_{-0.10}$
	$9.5 \leq \log(M_*) < 10$	33	$9.69^{+0.16}_{-0.10}$	$8.24^{+0.08}_{-0.02}$	$-8.17^{+0.16}_{-0.30}$
	$10 \leq \log(M_*) < 10.5$	24	$10.18^{+0.12}_{-0.07}$	$8.28^{+0.09}_{-0.07}$	$-8.76^{+0.26}_{-0.26}$
	$\log(M_*) > 10.5$	24	$10.89^{+0.25}_{-0.26}$	$8.46^{+0.03}_{-0.14}$	$-9.21^{+0.20}_{-0.12}$
$2.8 < z \leq 3.8$	$\log(M_*) < 8.5$	2	$8.41^{+0.02}_{-0.02}$	$7.93^{+0.01}_{-0.01}$	$-7.90^{+0.26}_{-0.26}$
	$8.5 \leq \log(M_*) < 9$	6	$8.82^{+0.12}_{-0.05}$	$7.88^{+0.22}_{-0.06}$	$-7.61^{+0.11}_{-0.16}$
	$9 \leq \log(M_*) < 9.5$	12	$9.35^{+0.07}_{-0.06}$	$8.12^{+0.04}_{-0.17}$	$-8.09^{+0.23}_{-0.20}$
	$9.5 \leq \log(M_*) < 10$	24	$9.71^{+0.14}_{-0.05}$	$8.16^{+0.01}_{-0.15}$	$-8.19^{+0.18}_{-0.42}$
	$10 \leq \log(M_*) < 10.5$	16	$10.12^{+0.18}_{-0.05}$	$8.21^{+0.05}_{-0.04}$	$-8.77^{+0.29}_{-0.19}$
	$\log(M_*) > 10.5$	8	$10.75^{+0.06}_{-0.14}$	$8.19^{+0.09}_{-0.02}$	$-8.86^{+0.38}_{-0.31}$

[a]Medians of values within each redshift bin; the upper and lower values correspond to the 75 per cent and 25 per cent quantile levels, respectively. We have not considered the AMAZE galaxy, LnA1689−2, at $z = 4.87$.

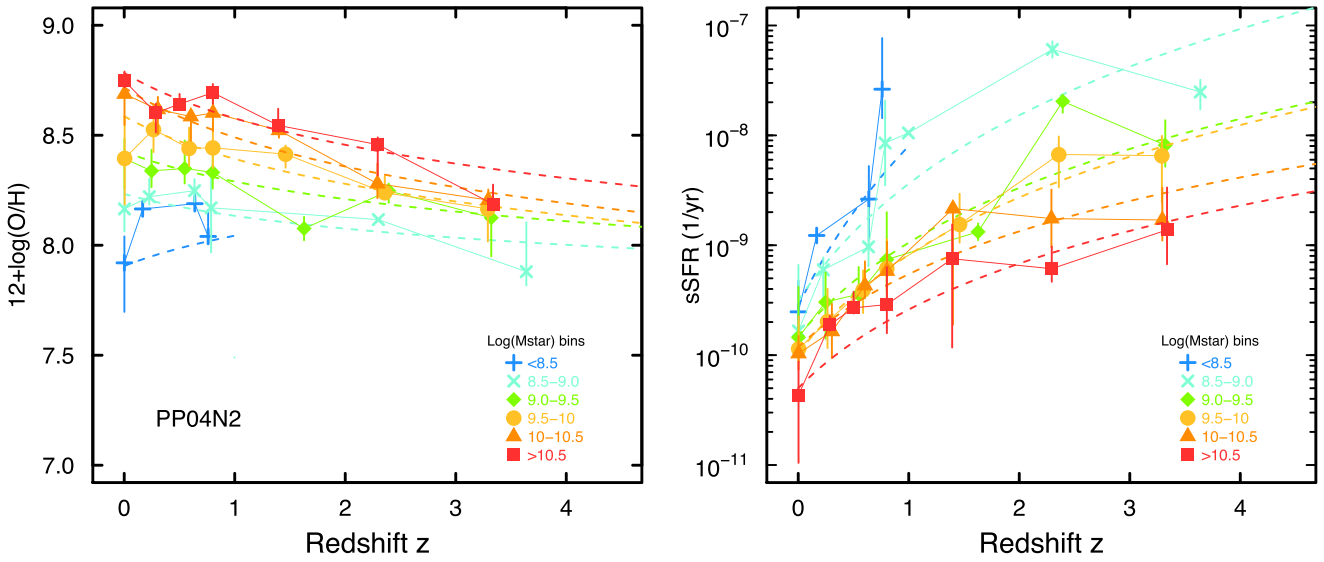

Figure 8. Binned measurements of 12+log(O/H) and sSFR as a function of redshift using the MEGA data set. As in the previous figures, the O/H calibration is PP04N2; the mass bins are shown in the lower-right corner. Error bars correspond to the 25th percentile of the vertical parameter within each mass bin. The curves are an approximation to the observed trends obtained by adopting the formulation of Karim et al. (2011) based on separable functions of M_* and z: sSFR, O/H $\propto M_*^{\beta}\,(1+z)^n$. The mean power-law indices, n, averaged over all mass bins (except the lowest one) are $\langle n\rangle(\mathrm{O/H}) = -0.57 \pm 0.17$ for 12+log(O/H) $\propto (1+z)^n$ (left-hand panel) and $\langle n\rangle(\mathrm{sSFR}) = 2.79 \pm 0.52$ for sSFR $\propto (1+z)^n$ (right).

Table 4. Fitted (PP04N2) O/H redshift variation of the MEGA data set[1].

Mass bin log($M_\odot$)	Number redshift points	a	b	Median residual	rms σ
8.5–9.0	77	8.23 ± 0.03	-0.33 ± 0.11	0.010	0.18
9.0–9.5	186	8.43 ± 0.02	-0.45 ± 0.07	0.002	0.15
9.5–10.0	349	8.59 ± 0.01	-0.64 ± 0.05	-0.002	0.14
10.5–10.5	132	8.72 ± 0.02	-0.75 ± 0.05	0.012	0.13
>10.5	100	8.78 ± 0.02	-0.68 ± 0.06	0.005	0.14

[1]Coefficients for robust fits to the individual data points (within each mass bin) of the form $12+\log(\mathrm{O/H}) = a + b\log(1+z)$; b corresponds to n(O/H) as described in the text.

12+log(O/H)(M_* = dex(9) $M_\odot$) $= 8.01 \pm 0.03$ within the highest ($z \sim 3$) redshift bin.

The slope β(O/H) for the MEGA data set at $z \sim 1.4$ of 0.23 ± 0.02 is slightly steeper than that by Yabe et al. (2014) who find $\beta = 0.15$, but shallower than the slope of ∼0.3 found by Liu et al. (2008) using PP04N2 in a similar redshift range (both samples are also included in the MEGA data set). The steeper slopes we find relative to Yabe et al. (2014) can be attributed to their use of a Salpeter IMF, rather than the Chabrier (2003) IMF used here. In the redshift range $z \sim$ 0.5–0.9, Cowie & Barger (2008) find an MZR slope of 0.13–0.17 using the KK04 and T04 O/H calibrations and a Salpeter IMF; this is also somewhat shallower than the PP04N2 $\beta = 0.24 \pm 0.02$ in a similar redshift range, but with the Chabrier IMF. The steeper slopes we find for the MEGA data set are consistent with those found by Zahid, Kewley & Bresolin (2011) for DEEP2 galaxies at $z \sim 0.8$ using the KK04 O/H calibration (and a Chabrier IMF). As discussed by Zahid et al. (2011), differences in fitting procedures are an important consideration in comparing slopes of the MZR, but the O/H calibration is also important. Kewley & Ellison (2008) illustrate that both the slope (at the low-mass end) and the absolute O/H determination depend strongly on the calibration. Thus, the consistency of the MZR slopes β relative to previous work lends confidence to our approach.

For the trends of sSFR with M_*, corresponding to the SFMS, averaging over all redshifts gives $\langle\beta\rangle(\mathrm{sSFR}) = -0.51 \pm 0.24$ (average and standard deviation over the individual redshift bins); the mean slope is poorly determined because of the (possibly spurious, see below) steepening towards high z. At $z \simeq 0$, we find $\beta(\mathrm{sSFR}) = -0.21 \pm 0.025$.[3] At $z \sim 0.25$, we find a steeper slope, $\beta(\mathrm{sSFR}) = -0.29 \pm 0.07$, roughly consistent with the sSFR versus M_* power-law index of ∼−0.4 estimated by Karim et al. (2011) and by Speagle et al. (2014) for $z \approx 0.3$. At $z \sim 3$, $\beta(\mathrm{sSFR}) = -0.64 \pm 0.09$; the observed steepening of β(sSFR) towards higher redshift evident in Fig. 9 is inconsistent with the results of Speagle et al. (2014) who find steeper slopes with increasing redshift in (log) SFR versus M_*, corresponding to shallower slopes in (log) sSFR.

Indeed, the MEGA data set does not show clear evidence for an SFMS within individual redshift bins (see Fig. 3); this could be because the galaxies at higher redshift are selected basically for a constant SFR (see Table 1) rather than a selection based on M_*. Such a selection can result in a basically flat trend of SFR with M_* (e.g. Erb et al. 2006b; Lee et al. 2013; Renzini & Peng 2015), which produces a steep dependence of sSFR with M_*, sSFR $\propto M_*^{-1}$, similar to the behaviour of the MEGA data set at high z. This is essentially a Malmquist bias since at low stellar masses, only galaxies with relatively high SFR are selected. Because the MEGA data set requires emission lines in order to measure metallicity spectroscopically, such an effect almost certainly plays an important role (e.g. Juneau et al. 2014). Ultimately, because of such selection effects, the MEGA data set may not be completely representative of the SFR–M_* correlations at high redshift. Nevertheless, it is the best data set currently available for assessing the evolution of the MZR.

[3] This slope is derived from all data at $z \simeq 0$, while the slope of -0.19 ± 0.02 in Section 4 is found from the LVL+KINGFISH galaxies only; the two slopes are in good agreement.

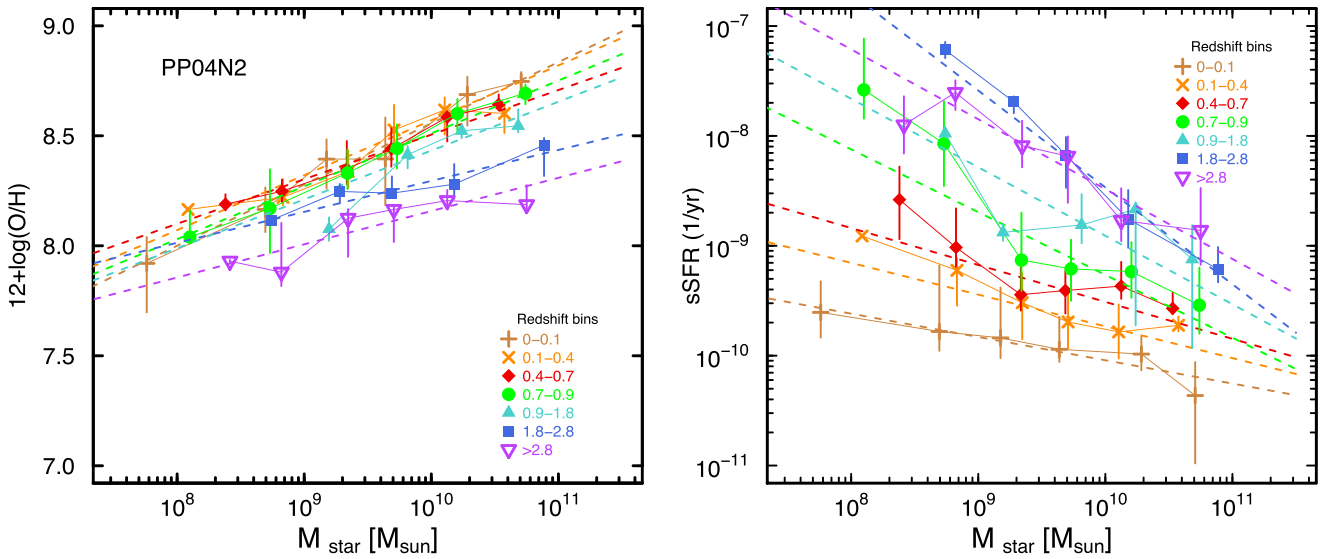

Figure 9. Binned measurements of 12+log(O/H) and sSFR as a function of M_* using the MEGA data set. As in the previous figures, the representative O/H calibration is PP04N2; the redshift bins are shown in the corners of the figures (see also Fig. 1). Error bars correspond to the 25th percentile of the vertical parameter within each redshift bin. As in Fig. 8, the curves are an approximation to the observed trends obtained by adopting the formulation of Karim et al. (2011) based on separable functions with the redshift trend given by $(1+z)^n$, and the M_* variation by M_*^{β}. The mean power-law indices, β, averaged over all redshift bins are $\langle\beta\rangle(\mathrm{O/H}) = 0.21 \pm 0.05$ for 12+log(O/H) $\propto {M_*}^{\beta(\mathrm{O/H})}$ (left-hand panel) and $\langle\beta\rangle(\mathrm{sSFR}) = -0.51 \pm 0.24$ for sSFR $\propto {M_*}^{\beta(\mathrm{sSFR})}$ (right).

5.3 Redshift invariance of the FPZ?

One way to assess the redshift invariance of the FPZ is by comparing the coefficients for redshift variation discussed above in Section 5.1 with those for the FPZ. We thus performed multi-variable linear regressions on the MEGA data set for 12+log(O/H) as a function of M_* and redshift, and the same for sSFR. Performing a robust fit,[4] we find (for the PP04N2 calibration)

$$12 + \log(\mathrm{O/H}) = 0.27\ \log(M_*) - 0.59\ \log(1+z) + 5.89 \qquad (2)$$

with a residual standard error of ∼0.15 dex, and

$$\log(\mathrm{sSFR}) = -0.29\ \log(M_*) + 2.88\ \log(1+z) - 7.16 \qquad (3)$$

with a residual standard error of ∼0.44 dex, The FPZ in equation (1) can be expressed as a function of sSFR, rather than SFR:

$$12 + \log(\mathrm{O/H}) = -0.14\ \log(\mathrm{sSFR}) + 0.23\ \log(M_*) + 4.82. \qquad (4)$$

By inserting the redshift variation of sSFR given by equation (3) in equation (4) for the FPZ, and comparing it with the redshift variation of O/H given by equation (2), we can compare the resulting difference equation term by term and assess the redshift invariance of the FPZ; we would expect ≈0 in such a case. The resulting coefficient for the difference (FPZ − z fits) of the log(M_*) term is 0.0004, consistent with 0. For log(1 + z), we find a difference of 0.178, roughly consistent with 0 to within the residual standard errors of the fits. The resulting difference for the constant term is −0.051, again consistent with 0 within the standard errors. Although this result pertains to PP04N2, similarly small difference coefficients are obtained for the D02 and PP04O3N2 calibrations. We thus conclude that the FPZ is approximately redshift invariant to within 0.15–0.16 dex (see Section 4.2); for typical galaxy populations, the increase of sSFR with redshift is compensated by the decrease in O/H (although see Wuyts et al. 2014).

Nevertheless, the log(1 + z) difference coefficient of ∼0.18 dex is slightly larger than would be expected given the residuals of the (PP04N2) FPZ, ∼0.16 dex. This implies that the FPZ is not a perfect formulation of the redshift evolution of metallicity. Therefore, to investigate the amplitude of the residual trend with redshift, in Fig. 10 we have plotted the FPZ O/H residuals versus redshift. The trend (shown by the solid line) is significant with

$$12 + \log(\mathrm{O/H}) - \mathrm{FPZ(PP04N2)} = (-0.048 \pm 0.006)\,z + 0.047 \pm 0.007. \qquad (5)$$

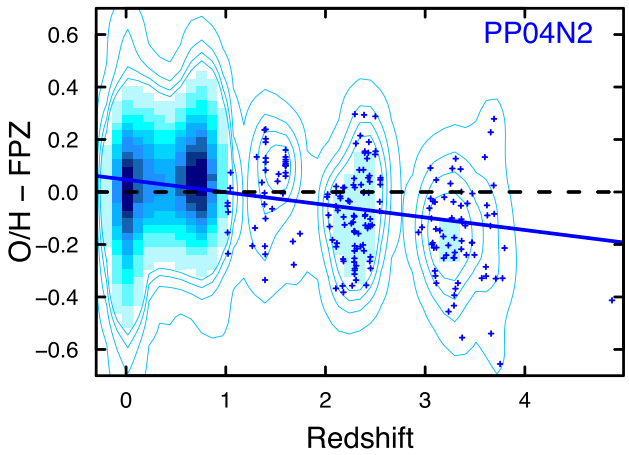

Figure 10. FPZ residuals for the MEGA data set with the PP04N2 calibration as a function of redshift. The colour scale corresponds to density of data points, and the contours show the full data set. Individual points are also plotted for $z \geq 1$. The horizontal dashed line guides the eye for zero residuals, while the solid line shows the best-fitting robust regression given by equation (5).

[4] For all statistical calculations, we use R, a free software environment for statistical computing and graphics, https://www.r-project.org/.

This implies that at $z \sim 3.5$, the FPZ predicts metallicities 12+log(O/H) that are roughly 0.17 dex too large. However, the residual standard error of the (PP04N2) fit in equation (5) is 0.16 dex, equivalent to the residuals of the FPZ itself; indeed, the spread of residuals at $z \sim 0$ is as large as or larger than the spread of residuals at $z \gtrsim 3$. Thus, while the current data suggest that the FPZ may not fully describe metallicity evolution (or its lack thereof related to SFR), the discrepancies are within the overall noise in the estimation. The data at $z \gtrsim 3$ are still relatively sparse, however, and more data with accurate metallicity measurements should help in confirming (or refuting) this conclusion.

6 DISCUSSION AND SUMMARY

The FPZ presented in Section 4.2 is based on the hypothesis that the curvature in the MZR at high stellar masses is compensated by the inflection in the SFMS. Our results show that this hypothesis is reasonably good, at least to within ∼0.16 dex in 12+log(O/H). Comparison of the FPZ with the FMR shows that both formulations adequately represent the mutual correlations of M_*, SFR, and O/H, but also that the O/H calibration is crucial; applying the FMR to arbitrary samples can result in metallicity offsets as large as −0.2 to −0.3 dex, compared with the three O/H calibrations considered here.

Some groups have concluded that at a given redshift or over a narrow range of redshifts the MZR does not depend on SFR (e.g. Wuyts et al. 2014; Sanders et al. 2015). However, the parameters of the MEGA sample in specific redshift intervals, given in Table 3, are comparable to the other samples used to draw these conclusions. It is likely that the broad parameter space spanned by the MEGA data set contributes to the differences in the outcome. The PCA analysis presented here could also play a role; indeed, if we fit the MEGA data with a simple multi-variable regression of 12+log(O/H) with respect to M_*, SFR, and redshift, we find very little dependence of O/H on SFR. This is because of the strong dependence of SFR (and sSFR) on redshift through the increasing normalization of the SFMS (e.g. Section 5). The mutual correlations of the variables underlying the FPZ must be taken into account for any analysis considering the MZR and its dependence on SFR.

In conclusion, we have compiled a new MEGA data set consisting of ∼1000 galaxies taken from 19 individual samples spanning a wide range of stellar masses, SFRs, and metallicities and covering redshifts from $z \simeq 0$ to $z \sim 3.7$. In addition to larger numbers of high-z galaxies, the main improvement of this data set over that of Hunt et al. (2012) is the common O/H calibrations derived for the MEGA galaxies. The main results are as follows.

(i) After examining the mutual correlations among these parameters, a PCA of the MEGA data set shows that the 3D parameter space can be described by a plane, dubbed the FPZ.

(ii) The functional form of the (PP04N2) FPZ is given by $12 + \log(\mathrm{O/H}) = -0.14 \log(\mathrm{SFR}) + 0.37 \log(M_*) + 4.82$ over the entire mass and redshift range of the MEGA data set.

(iii) The mean O/H residuals of the FPZ over the MEGA data set are 0.16 dex (for the PP04N2 calibration, slightly larger for D02 and PP04O3N2); such residuals are smaller than those found previously, and consistent with trends found in smaller galaxy samples with more limited ranges in M_*, SFR, and O/H.

(iv) The FPZ is also found to be roughly invariant with redshift enabling an estimation of metallicity accurate to within 0.16 dex over roughly five orders of magnitude in M_*, from $\gtrsim 10^6$ to $\sim 10^{11}$ $M_\odot$, up to $z \sim 3.7$. An additional correction for redshift may be employed to increase slightly the accuracy of O/H estimates from the FPZ for $z \gtrsim 2$ (see equation 5).

ACKNOWLEDGEMENTS

We acknowledge the anonymous referee whose insightful comments greatly improved the paper. We thank Giovanni Cresci and Chun Ly for passing us their SDSS10, ZCOSMOS, and DEEP2 data in electronic form, and are grateful to the DAVID network (http://wiki.arcetri.astro.it/DAVID/WebHome) for fostering a fruitful collaborative environment. PD gladly acknowledges funding from the EU COFUND Rosalind Franklin programme.

REFERENCES

Amorín R. O., Pérez-Montero E., Vílchez J. M., 2010, ApJ, 715, L128
Andrews B. H., Martini P., 2013, ApJ, 765, 140
Bell E. F., de Jong R. S., 2001, ApJ, 550, 212
Berg D. A. et al., 2012, ApJ, 754, 98
Berg D. A., Skillman E. D., Croxall K. V., Pogge R. W., Moustakas J., Johnson-Groh M., 2015, ApJ, 806, 16
Binette L., Matadamas R., Hägele G. F., Nicholls D. C., Magris C. G., Peña-Guerrero M. Á., Morisset C., Rodríguez-González A., 2012, A&A, 547, A29
Blanc G. A., Kewley L., Vogt F. P. A., Dopita M. A., 2015, ApJ, 798, 99
Bresolin F., 2007, ApJ, 656, 186
Brinchmann J., Charlot S., White S. D. M., Tremonti C., Kauffmann G., Heckman T., Brinkmann J., 2004, MNRAS, 351, 1151
Brown M. J. I. et al., 2014, ApJS, 212, 18
Cairós L. M., Caon N., Zurita C., Kehrig C., Roth M., Weilbacher P., 2010, A&A, 520, A90
Calzetti D. et al., 2010, ApJ, 714, 1256
Cannon J. M., Walter F., Skillman E. D., van Zee L., 2005, ApJ, 621, L21
Cardamone C. et al., 2009, MNRAS, 399, 1191
Chabrier G., 2003, PASP, 115, 763
Cook D. O. et al., 2014, MNRAS, 445, 899
Cowie L. L., Barger A. J., 2008, ApJ, 686, 72
Cresci G., Mannucci F., Sommariva V., Maiolino R., Marconi A., Brusa M., 2012, MNRAS, 421, 262
Cullen F., Cirasuolo M., McLure R. J., Dunlop J. S., Bowler R. A. A., 2014, MNRAS, 440, 2300
Dale D. A. et al., 2007, ApJ, 655, 863
Dale D. A. et al., 2009, ApJ, 703, 517
Davis M. et al., 2003, Proc. SPIE, 4834, 161
Dayal P., Ferrara A., Dunlop J. S., 2013, MNRAS, 430, 2891
de los Reyes M. A. et al., 2015, AJ, 149, 79
Denicoló G., Terlevich R., Terlevich E., 2002, MNRAS, 330, 69 (D02)
Dopita M. A., Pereira M., Kewley L. J., Capaccioli M., 2002, ApJS, 143, 47
Draine B. T., Li A., 2007, ApJ, 657, 810
Elbaz D. et al., 2007, A&A, 468, 33
Elbaz D. et al., 2011, A&A, 533, A119
Ellison S. L., Patton D. R., Simard L., McConnachie A. W., 2008, ApJL, 672, L107
Engelbracht C. W., Rieke G. H., Gordon K. D., Smith J.-D. T., Werner M. W., Moustakas J., Willmer C. N. A., Vanzi L., 2008, ApJ, 678, 804
Epinat B. et al., 2009, A&A, 504, 789
Erb D. K., Shapley A. E., Pettini M., Steidel C. C., Reddy N. A., Adelberger K. L., 2006a, ApJ, 644, 813
Erb D. K., Steidel C. C., Shapley A. E., Pettini M., Reddy N. A., Adelberger K. L., 2006b, ApJ, 647, 128
García-Rojas J., Esteban C., 2007, ApJ, 670, 457

Gavazzi G. et al., 2015, A&A, 580, A116
Gil de Paz A., Madore B. F., Pevunova O., 2003, ApJS, 147, 29
Grazian A. et al., 2006, A&A, 449, 951
Grossi M. et al., 2015, A&A, 574, A126
Guseva N. G., Papaderos P., Izotov Y. I., Green R. F., Fricke K. J., Thuan T. X., Noeske K. G., 2003a, A&A, 407, 91
Guseva N. G., Papaderos P., Izotov Y. I., Green R. F., Fricke K. J., Thuan T. X., Noeske K. G., 2003b, A&A, 407, 105
Guseva N. G., Izotov Y. I., Stasińska G., Fricke K. J., Henkel C., Papaderos P., 2011, A&A, 529, A149
Guseva N. G., Izotov Y. I., Fricke K. J., Henkel C., 2012, A&A, 541, A115
Henry A., Martin C. L., Finlator K., Dressler A., 2013, ApJ, 769, 148
Hunt L. K., Vanzi L., Thuan T. X., 2001, A&A, 377, 66
Hunt L. K., Giovanardi C., Helou G., 2002, A&A, 394, 873
Hunt L. K., Dyer K. K., Thuan T. X., Ulvestad J. S., 2004, ApJ, 606, 853
Hunt L. K., Dyer K. K., Thuan T. X., 2005, A&A, 436, 837
Hunt L. K., Thuan T. X., Izotov Y. I., Sauvage M., 2010, ApJ, 712, 164
Hunt L. et al., 2012, MNRAS, 427, 906
Izotov Y. I., Thuan T. X., 2004, ApJ, 602, 200
Izotov Y. I., Stasińska G., Meynet G., Guseva N. G., Thuan T. X., 2006, A&A, 448, 955
Izotov Y. I., Thuan T. X., Stasińska G., 2007, ApJ, 662, 15
Izotov Y. I., Guseva N. G., Fricke K. J., Papaderos P., 2009, A&A, 503, 61
Izotov Y. I., Guseva N. G., Thuan T. X., 2011, ApJ, 728, 161
Izotov Y. I., Thuan T. X., Privon G., 2012, MNRAS, 427, 1229
James P. A. et al., 2004, A&A, 414, 23
James B. L., Tsamis Y. G., Barlow M. J., 2010, MNRAS, 401, 759
Johnson K. E., Hunt L. K., Reines A. E., 2009, AJ, 137, 3788
Juneau S. et al., 2014, ApJ, 788, 88
Karim A. et al., 2011, ApJ, 730, 61
Kauffmann G. et al., 2003, MNRAS, 341, 54
Kennicutt R. C., Jr, Lee J. C., Funes S. J., José G., Sakai S., Akiyama S., 2008, ApJS, 178, 247
Kennicutt R. C. et al., 2011, PASP, 123, 1347
Kewley L. J., Dopita M. A., 2002, ApJS, 142, 35 (KD02)
Kewley L. J., Ellison S. L., 2008, ApJ, 681, 1183
Kniazev A. Y., Grebel E. K., Hao L., Strauss M. A., Brinkmann J., Fukugita M., 2003, ApJ, 593, L73
Kniazev A. Y., Pustilnik S. A., Grebel E. K., Lee H., Pramskij A. G., 2004, ApJS, 153, 429
Kobulnicky H. A., Kewley L. J., 2004, ApJ, 617, 240 (KK04)
Kobulnicky H. A., Skillman E. D., 1996, ApJ, 471, 211
Kobulnicky H. A., Skillman E. D., 1997, ApJ, 489, 636
Lagos P., Papaderos P., Gomes J. M., Smith Castelli A. V., Vega L. R., 2014, A&A, 569, A110
Lamareille F. et al., 2009, A&A, 495, 53
Lara-López M. A. et al., 2010, A&A, 521, L53
Lara-López M. A., López-Sánchez Á. R., Hopkins A. M., 2013, ApJ, 764, 178
Lee H., Skillman E. D., Cannon J. M., Jackson D. C., Gehrz R. D., Polomski E. F., Woodward C. E., 2006, ApJ, 647, 970
Lee J. C. et al., 2009, ApJ, 706, 599
Lee J. C. et al., 2011, ApJS, 192, 6
Lee N. et al., 2013, ApJ, 778, 131
Lee N. et al., 2015, ApJ, 801, 80
Leroy A. K. et al., 2012, AJ, 144, 3
Lilly S. J. et al., 2009, ApJS, 184, 218
Liu X., Shapley A. E., Coil A. L., Brinchmann J., Ma C.-P., 2008, ApJ, 678, 758
Liu X.-W., Storey P. J., Barlow M. J., Clegg R. E. S., 1995, MNRAS, 272, 369
Liu X.-W., Storey P. J., Barlow M. J., Danziger I. J., Cohen M., Bryce M., 2000, MNRAS, 312, 585
Liu X.-W., Luo S.-G., Barlow M. J., Danziger I. J., Storey P. J., 2001, MNRAS, 327, 141
López-Sánchez Á. R., Esteban C., 2008, A&A, 491, 131
Ly C., Rigby J. R., Cooper M., Yan R., 2015, ApJ, 805, 45
McGaugh S. S., 1991, ApJ, 380, 140
McGaugh S. S., Schombert J. M., 2014, AJ, 148, 77
Maiolino R. et al., 2008, A&A, 488, 463
Mannucci F. et al., 2009, MNRAS, 398, 1915
Mannucci F., Cresci G., Maiolino R., Marconi A., Gnerucci A., 2010, MNRAS, 408, 2115
Mannucci F., Salvaterra R., Campisi M. A., 2011, MNRAS, 414, 1263
Marble A. R. et al., 2010, ApJ, 715, 506
Mattsson L., Pilyugin L. S., Bergvall N., 2011, MNRAS, 415, L54
Moustakas J., Kennicutt R. C., Jr, 2006, ApJS, 164, 81
Moustakas J., Kennicutt R. C., Jr, Tremonti C. A., Dale D. A., Smith J.-D. T., Calzetti D., 2010, ApJS, 190, 233
Murphy E. J. et al., 2011, ApJ, 737, 67
Nicholls D. C., Dopita M. A., Sutherland R. S., 2012, ApJ, 752, 148
Nicholls D. C., Dopita M. A., Sutherland R. S., Kewley L. J., Palay E., 2013, ApJS, 207, 21
Noeske K. G. et al., 2007, ApJ, 660, L43
Norris M. A., Meidt S., Van de Ven G., Schinnerer E., Groves B., Querejeta M., 2014, ApJ, 797, 55
Oliver S. et al., 2010, MNRAS, 405, 2279
Onodera M. et al., 2016, ApJ, 822, 42
Osterbrock D. E., Ferland G. J., 2006, Astrophysics of Gaseous Nebulae and Active Galactic Nuclei, 2nd edn. University Science Books, Sausalito, CA
Peimbert M., 1967, ApJ, 150, 825
Peimbert A., Peimbert M., 2010, ApJ, 724, 791
Peimbert M., Storey P. J., Torres-Peimbert S., 1993, ApJ, 414, 626
Peña-Guerrero M. A., Peimbert A., Peimbert M., 2012, ApJ, 756, L14
Pérez-Montero E., Díaz A. I., 2005, MNRAS, 361, 1063
Pérez-Montero E., García-Benito R., Hägele G. F., Díaz Á. I., 2010, MNRAS, 404, 2037
Pérez-Montero E. et al., 2011, A&A, 532, A141
Pettini M., Pagel B. E. J., 2004, MNRAS, 348, L59 (PP04)
Pustilnik S. A., Pramskij A. G., Kniazev A. Y., 2004, A&A, 425, 51
Queyrel J. et al., 2009, A&A, 506, 681
Renzini A., Peng Y.-j., 2015, ApJ, 801, L29
Roennback J., Bergvall N., 1995, A&A, 302, 353
Rosa-González D., Schmitt H. R., Terlevich E., Terlevich R., 2007, ApJ, 654, 226
Salim S. et al., 2007, ApJS, 173, 267
Salim S., Lee J. C., Ly C., Brinchmann J., Davé R., Dickinson M., Salzer J. J., Charlot S., 2014, ApJ, 797, 126
Sanders R. L. et al., 2015, ApJ, 799, 138
Schmitt H. R., Calzetti D., Armus L., Giavalisco M., Heckman T. M., Kennicutt R. C., Jr, Leitherer C., Meurer G. R., 2006, ApJS, 164, 52
Shapley A. E., Erb D. K., Pettini M., Steidel C. C., Adelberger K. L., 2004, ApJ, 612, 108
Shapley A. E., Coil A. L., Ma C.-P., Bundy K., 2005, ApJ, 635, 1006
Shi F., Kong X., Li C., Cheng F. Z., 2005, A&A, 437, 849
Skibba R. A. et al., 2011, ApJ, 738, 89
Smith B. J., Hancock M., 2009, AJ, 138, 130
Speagle J. S., Steinhardt C. L., Capak P. L., Silverman J. D., 2014, ApJS, 214, 15
Stasińska G., 2005, A&A, 434, 507
Steidel C. C., Adelberger K. L., Giavalisco M., Dickinson M., Pettini M., 1999, ApJ, 519, 1
Steidel C. C. et al., 2014a, ApJ, 795, 165
Steidel C. C. et al., 2014b, ApJ, 795, 165
Thuan T. X., Izotov Y. I., 2005, ApJS, 161, 240
Tremonti C. A. et al., 2004, ApJ, 613, 898 (T04)
Troncoso P. et al., 2014, A&A, 563, A58
Tsamis Y. G., Barlow M. J., Liu X.-W., Storey P. J., Danziger I. J., 2004, MNRAS, 353, 953
Vigroux L., Stasińska G., Comte G., 1987, A&A, 172, 15
Wen X.-Q., Wu H., Zhu Y.-N., Lam M. I., Wu C.-J., Wicker J., Zhao Y.-H., 2013, MNRAS, 433, 2946

Whitaker K. E. et al., 2014, ApJ, 795, 104
Wuyts S. et al., 2011, ApJ, 742, 96
Wuyts E. et al., 2014, ApJ, 789, L40
Wyder T. K. et al., 2007, ApJS, 173, 293
Xia L. et al., 2012, AJ, 144, 28
Yabe K. et al., 2012, PASJ, 64, 60
Yabe K. et al., 2014, MNRAS, 437, 3647
Yates R. M., Kauffmann G., 2014, MNRAS, 439, 3817
Yates R. M., Kauffmann G., Guo Q., 2012, MNRAS, 422, 215
Zahid H. J., Kewley L. J., Bresolin F., 2011, ApJ, 730, 137
Zahid H. J., Dima G. I., Kewley L. J., Erb D. K., Davé R., 2012, ApJ, 757, 54
Zahid H. J. et al., 2014, ApJ, 792, 75
Zhao Y., Gao Y., Gu Q., 2010, ApJ, 710, 663
Zibetti S., Charlot S., Rix H.-W., 2009, MNRAS, 400, 1181

This paper has been typeset from a TEX/LATEX file prepared by the author.